Application of handheld ED-XRF for high-resolution chemostratigraphy in texturally homogeneous carbonate mudstones: Salina A-1 Carbonate (Silurian), Michigan Basin

Matthew A. Hemenway, M.S.

Western Michigan University, 2018

Handheld energy dispersive x-ray fluorescence spectrometry (ED-XRF) is routinely used to observe elemental variability in fine-grained siliciclastics but has been applied rarely in fine-grained carbonates. Here, ED-XRF chemostratigraphy is utilized in the texturally homogenous, mudstones of the Silurian A-1 Carbonate (A-1C), Michigan Basin. Previous studies on the A-1C focused on the stratigraphic relationship with the underlying Niagaran reefs, so little is known about the geological variability in the basin center. In this study, high-resolution elemental data from nine cores were integrated with petrographic and mineralogical observations to evaluate two hypotheses: (1) Texturally homogeneous, basin-center mudstones in the A-1C have spatially correlative elemental signatures (i.e. chemofacies); (2) Elemental variations reflect temporal changes in relative sea-level, redox conditions, and sedimentation rate.

ED-XRF measured elemental abundances of redox-sensitive elements (Mo, Ni, Cu) are consistently low throughout the basin, suggesting oxic conditions during deposition. Spatially correlative temporal variations in Si, Al, K, and S are observed between basin-center wells. High abundances of Si, Al, and K are associated with siliciclastic minerals and are interpreted to reflect intensification of clastic sedimentation caused by sea-level drawdown. Associated S increases reflects a higher abundance of anhydrite, which is interpreted as diagenetically altered gypsum that was deposited during periods of low relative sea-level. Chemofacies successions indicate six low-order transgressive-regressive cycles and up to fourteen high-order cycles. These findings demonstrate the ability of ED-XRF to provide geologically relevant elemental data that can be used to refine sequence stratigraphic interpretations in fine-grained carbonates.

Application of handheld ED-XRF for high-resolution chemostratigraphy in texturally homogeneous carbonate mudstones: Salina A-1 Carbonate (Silurian), Michigan Basin

by

Matthew A. Hemenway

A thesis submitted to the Graduate College in partial fulfillment
of the requirements for the degree of Master of Science,
Department of Geological and Environmental Sciences
Western Michigan University
May 2018

Thesis Committee:

Stephen Kaczmarek, Ph.D.
William Harrison III, Ph.D.
Peter Voice, Ph.D.
Jay Zambito, Ph.D.

ACKNOWLEDGMENTS

I would like to acknowledge the people who have helped me along the way in my studies. I would like to thank my wife, Erin, for her unwavering support and patience while I pursue my goals. My advisor, Steve Kaczmarek, for his relentless energy and for teaching me how to be a skeptical scientist. My committee members, Bill Harrison, Peter Voice, and Jay Zambito, for their critical eye and vast, collective knowledge. A personal thank you to Linda Harrison and Jennifer Trout for making MGRRE a second home for me over the past 3 years. To the Department of Geological and Environmental Sciences for a graduate assistantship position. And to my parents, Tim and Jane Hemenway, who first introduced me to scientific discovery in the pond behind our house. Thank you all for your support.

-Matthew A. Hemenway

TABLE OF CONTENTS

LIST OF TABLES

LIST OF FIGURES

List of Figures - continued

INTRODUCTION

Chemostratigraphic analysis utilizing temporal variations in the elemental composition of sedimentary rocks has become common practice for inferring paleoenvironments and building stratigraphic frameworks (e.g., Caplan & Bustin 1998, Algeo & Lyons 2006, Rowe et al. 2009, Ratcliffe et al. 2010, Algeo & Rowe 2012, Rowe et al. 2012, Dahl et al. 2013, Coimbra et al. 2015, Craigie 2015, Turner et al. 2016, Ibrahim et al. 2016, Ratcliffe et al. 2017, Rine et al. 2017, Craigie 2018). Most of these studies relied on conventional spectrometry and spectroscopy tools, such as ICP-MS, ICP-OES, benchtop WD-XRF, to acquire elemental data at a meter to sub-meter resolution. More recently, handheld x-ray fluorescence spectrometry (ED-XRF) has been utilized as a tool for more cost- and time-effective, non-destructive acquisition of large, high-resolution (cm scale) geochemical datasets (Rowe et al. 2009, Rowe et al. 2012, Dahl et al. 2013, Turner et al. 2016, Rine et al. 2017). The first studies to use ED-XRF in sedimentary basins did so with the goal of investigating the elemental variation of otherwise homogeneous siliciclastic mudrocks (Rowe et al. 2009, Rowe et al. 2012, Dahl et al. 2013, Turner et al. 2016). These studies interpreted temporal elemental variations as proxies for variations in the source of clastic sediments, shoreline proximity, and redox conditions. Application of ED-XRF to investigate carbonates, however, has been limited (e.g., Quye-Sawyer et al. 2015, Rine et al. 2017). Thus, it is less clear whether elemental proxies used in clastic systems have the same application in fine-grained carbonates.

In a recent study by Rine et al. (2017), ED-XRF elemental data were used in combination with detailed core descriptions to construct a sequence stratigraphic framework of the Salina (Silurian) A-1 Carbonate (A-1C) in the Michigan Basin. The A-1C

was previously described as an algal and microbial carbonate mudstone (Budros and Briggs 1977). Previous studies focused primarily on the stratigraphic relationship of the A-1C with the underlying Niagaran reef reservoirs near the basin margin (Gill 1973; Budros and Briggs 1977; Obermajer et al. 2000). Rine et al. (2017) developed a new sequence stratigraphic framework for the A-1C by comparing lithofacies successions from sixteen cores throughout the basin with ED-XRF elemental data from three of those cores. Lithofacies successions and petrographic observations were used to make relative sea-level interpretations, which were supported by variations in common siliciclastic proxy elements (Bhatia and Crook 1986, Pearce and Jarvis 1992, Banner 1995, Pearce et al. 1999, Sageman and Lyons 2004, Tribovillard et al. 2006, Algeo and Rowe 2012). Rine et al. (2017) correlated an anhydrite-rich interval, known as the "Rabbit Ears Anhydrite" (REA), to multiple wells in different interpreted paleogeographic locations in the basin. Additionally, they argued that the REA bifurcates the A-1C into an upper and lower unit. Despite finding it difficult to correlate Si, K, Al, Fe, Mo, Ni, Ca, and Mg between the margin and the central basin, Rine et al. (2017) noted that at the coarse-scale, there was good agreement between the interpreted relative sea-level changes derived from lithofacies successions and the elemental record. More specifically, they suggested that elevated levels of S, Si, Al, K, Ni, and Mo were proxies for lowstand stages and were associated with shallowing facies successions at the basin-margin. The influence of lithofacies changes on elemental variation or the mineral association of elements were not examined. While there is no reason to suspect that the interpretations of Rine et al. (2017) are invalid, the principles used to interpret ED-XRF derived elemental data in carbonates

remain largely untested, specifically the use of elevated abundances of Ni and Mo as proxies for redox conditions.

Understanding the controls on A-1C deposition is important, as the A-1C considered the likely source rock and partial reservoir for the Niagaran reef play in the Michigan Basin (Gardner & Bray 1984, Obermajer et al. 2000, Garrett 2016). The generation, accumulation, and preservation of organic matter in sediments is governed by multiple processes that reflect the biology, water chemistry and circulation, and redox conditions (Demaison & Moore 1980). Recognition of spatial and temporal paleoenvironmental changes are valuable information when evaluating source rock quality and quantity (i.e. potential hydrocarbon volumes).

What is still unknown, however, is (1) what is the extent of geochemical variability in basin-center A-1C mudstones and (2) what are the fundamental sedimentological and diagenetic controls on elemental variations observed in the basin-center mudstones?

In this study, high-resolution (~2.5 cm) ED-XRF elemental data from basin-center wells were integrated with mineralogical data to evaluate two hypotheses:

1) Texturally homogeneous basin-center mudstones in the A-1C have spatially correlative elemental signatures (i.e. chemofacies).

2) Elemental variations reflect temporal changes in relative sea-level, redox conditions, and sedimentation rate.

METHODS

ED-XRF

Nine cores, consisting of A-1C mudstones, were analyzed with ED-XRF (Figure 1, Table 1). Four cores (Bruske, KH 1054, Dalrymple, and Dow) are located in the basin center, three cores along the basin slope (St. Christensen, Schultz and Mutton), and 2 cores from the basin margin (Dreves and David). The Dreves, Bruske, KH 1054, St. Christensen, David, Schultz, and Mutton were considered the key wells in this study. For the Dalrymple and Dow, elemental data was only collected at locations where TOC was measured and not the entire length of the core, as the cored interval missed large sections of the A-1C.

Core preparation for ED-XRF analysis included slabbing and cleaning the core to remove residue from drilling fluids and re-precipitated halite that commonly formed on the slabbed surface. Cores were cleaned with a Dremel power tool to mechanically remove the top ~1 mm of the slabbed core face with coarse-grit, Al_2O_3 sanding bands. Slabbed surfaces were then cleaned with compressed air and scrubbed with a small amount of de-ionized water to remove residual halite re-precipitated from the underlying and overlying evaporite formations.

Table 1: Wells with cores used in this study listed by well ID, name, permit number, operating company, and location

Well ID	Name (Abbr)	Permit Number	Operating Company	Location (County, Township, Lat-Long)
Well 1	Dreves, Carl 1 (Dreves)	27454	CMS Oil and Gas Co.	Grand Traverse, East Bay, 44.6849N-85.5547W
Well 2	Bruske 1-26A (Bruske)	59271	Ranch Production LLC	Osceola, Lincoln, 43.9185N-85.4794W
Well 3	Kalium Hersey 1054 (KH 1054)	00387	Cargill Salt – Hersey	Osceola, Hersey, 43.8398N-85.3619W
Well 4	State Orange & Christensen 1-21P (St. Christensen)	60614	Rosetta Resources Michigan LP	Ionia, Orange, 42.8917N-85.0165W
Well 5	David, Donald L. 1 (David)	28363	BP America Production Co	Eaton, Brookfield, 42.4952N-84.8024W
Well 6	Schultz 1-36 (Schultz)	59112	Whiting Oil and Gas Corp	Sanilac, Bridgehampton, 43.4414N-82.6407W
Well 7	Mutton, William 1 (Mutton)	24490	Phillips Petroleum Co	Sanilac, Sanilac, 43.4389N-82.6111W
Well 8	Dow Chemical 8SM (Dow)	00286	Dow Chemical Co	Midland, Midland, 43.5996N-84.2435W
Well 9	Dalrymple et al 1-16 (Dalrymple)	34537	Dart Oil and Gas Corp	Roscommon, Roscommon, 44.2967N-84.796W

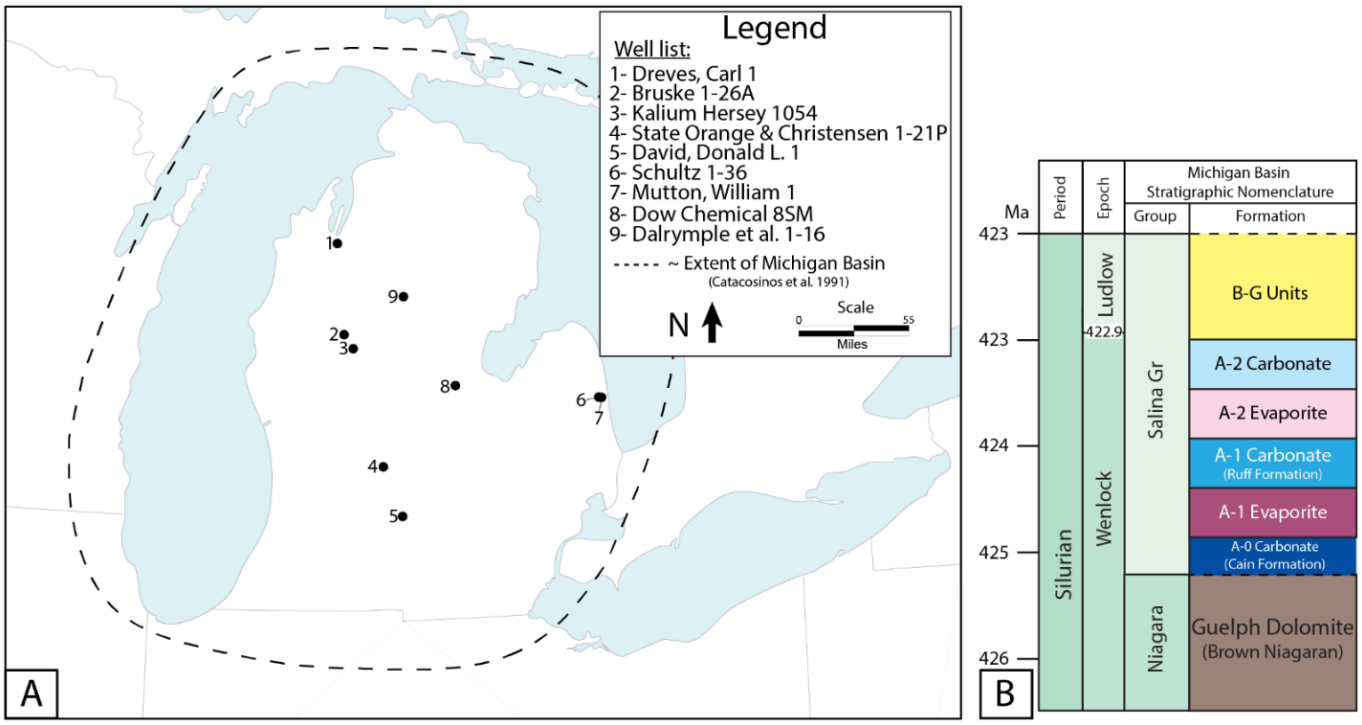

Figure 1: A) Map of the study area in the Michigan Basin including wells used in this study. B) Silurian stratigraphic column and Michigan Basin stratigraphic nomenclature (modified from Rine et al. 2017).

Prepared core slabs were then immediately analyzed with the Bruker Tracer IV-SD handheld ED-XRF at a 2.5 cm vertical sampling rate. The only exception was the Dreves, which was analyzed at a 15 cm interval. Each sample location was scanned twice: once for major elements and once for trace elements, for a total of over 9,000 individual ED-XRF measurements. Major elements, including Mg, Al, Si, P, S, K, Ca, and V, were collected in low energy mode (15kV cathode voltage, 35 µA cathode current) with no instrument filter and a 0.1 liter per minute helium atmosphere purge for 60 seconds. Trace elements, including Ti, Cr, Mn, Fe, Co, Ni, Cu, Zn, Ga, As, Se, Sr, Y, Zr, Nb, Mo, Ba, Pb, Th, and U, were collected in high energy mode (40 kV cathode voltage and 40 µA cathode current) with a filter composed of 0.006" Cu, 0.001" Ti, and 0.012" Al in ambient atmosphere for 90 seconds.

ED-XRF spectra were checked for anomalous peak values and, if necessary, reanalyzed for quality assurance. Raw spectra were processed using Bruker Artax Spectra software. Artax is a proprietary software that statistically corrects for intra-elemental peak interference and background scatter for measurements using Bayesian deconvolution. This is accomplished by applying Bayesian algorithms to create a deconvoluted, "baseline" spectrum by manually identifying elements present in a spectrum. Artax subtracts the baseline from the measured spectrum and exports each element in photon counts.

Principle Component Analysis (PCA)

Processed photon counts for each element were imported into Schlumberger TechLog Heterogenous Rock Analysis clustering module to conduct principle component analysis (PCA). In general, PCA was used to statically assign chemofacies classes based

on relationship between input elements, to provide an objective designation of chemofacies. The goal is to increase similarity within a given class and maximize differences between classes. PCA determines the number of principle components (i.e. variables) needed to characterize 95% of the variation in a set of data and allocates data points into related clusters such that intra-cluster variation is minimized, and extra-cluster variation is maximized (Abdi & Williams 2010). Classification can be done manually, but PCA provides a more objective analysis of chemofacies that is less subject to bias from geological interpretations. The input variables and number of clusters (i.e. chemofacies) was manually specified.

PCA was applied to ED-XRF elemental data in key wells to classify chemofacies for both Si, Al, and K (SAK-CF) and S (S-CF). Calculated moving average curves over 0.5 ft for Si, Al, K, and S were used as the input variables, and both analyses were conducted with 2, 3, 4, and 5 clusters. The best fit for clusters was determined through comparison of average distance ratio (*s(i)*) for each data point using the mean intra-cluster distance (*a)* and the mean distance to the nearest neighboring cluster (*b*) (Equation 1) (Rousseeuw 1987).

$$s(i) = \begin{cases} 1 - \frac{a}{b}, & if\ a < b \\ 0, & if\ a = b \\ \frac{b}{a} - 1, & if\ a > b \end{cases} \qquad \textit{Equation 1}$$

ED-XRF measurements with a calculated *s(i)* close to 1 suggests a good fit for their assigned cluster while those with a *s(i)* approaching -1 suggests a poor fit for their assigned cluster.

RockEval Pyrolysis

To evaluate the association between trace elements and organic matter, 117 total organic carbon (TOC) measurements were publicly available at the Michigan Geological Repository for Research and Education (MGRRE) for the Bruske, David, Schultz, Mutton, Dalrymple, and Dow. These TOC measurements were collected by various exploration companies with programmed RockEval Pyrolysis and LECO carbon analyzer from core plugs or chips samples. These two methods both measure geochemical variables relating to organic richness of source rocks and degree of thermal maturation, such as TOC, S1, S2, S3, and T_{max}. These measurements were then compared with trace elements Ni, Cu, Mo, Zn, Co, V, and Mn measured with ED-XRF at the same location.

X-Ray Diffractometry

X-ray diffraction (XRD) was used to evaluate the relationship between mineralogy and elemental abundances measured with ED-XRF. Calculated weight percent (wt%) mineralogy from XRD for 19 core plugs were publicly available at MGRRE for St. Christensen. These samples were analyzed by Weatherford Laboratories with standard XRD techniques to calculate wt% for a suite of common sedimentary minerals.

Scanning Electron Microscope (SEM)

The JEOL JSM-IT100 InTouchScope at WMU was used to obtain SEM photomicrographs of fine-grained siliciclastics for two samples from St. Christensen. A core sample measuring ~0.5 cm was cleaned with compressed air and mounted on an aluminum specimen stub with electrically conductive carbon tape. The mounted sample was made electrically conductive by coating the sample with 5- 10 nm of carbon using a

carbon fiber thermal evaporator (Fullam Inc.). This reduced electron charge build-up on the surface of the sample during analysis and maximized image quality. Samples were analyzed at 20 kV accelerating voltage and 10mm working distance. A built-in energy-dispersive spectrometry (EDS) was used to identify the elemental composition of specific sections of the sample.

RESULTS AND INTERPRETATION

ED-XRF Elemental Profiles

The principal geochemical data collected in this study are displayed as ED-XRF elemental profiles for key wells (Figures 2-8). Elements reported include Mg, Ca, Al, Si, K, Fe, Co, Ti, Sr, S, Ni, Cu, V, Mo, Zn, and Mn. Elemental profiles for each well are presented in separate tracks with elemental abundances (measured in photon counts) increasing to the right. In each track individual ED-XRF measurements are plotted as data points and as a continuous curve that represents the calculated moving average over a 0.5 ft interval. The scale for each element in photon counts was determined based on the photon count range observed by Rowe et al. (2012) (see Appendix 2 for details). Displayed to the right of each profile are the observed lithofacies.

For quality control of ED-XRF measurements, the standard error was determined by analyzing a sample 30 consecutive times to calculate the standard deviation of photon counts for each element. Table 2 displays the standard deviation in photon counts for each element reported in this study (Data courtesy of Mohammed Al-Musawi).

Figures 2-8 show that elemental abundances in the A-1C are highly variable with respect to their frequency and magnitude. Based on the characteristics of elemental signatures, elements were organized into 3 geochemical groups. *Group 1* elements, which include Si, Al, K, and S, are characterized by abundances exhibiting correlative trends. *Group 2* elements, which include Ca, Mg, Fe, Sr, V, Ti, and Zn, are characterized by elemental abundances exhibiting non-correlative trends. *Group 3*

elements, which include Co, Ni, Cu, Mo, and Mn, are characterized by elemental abundances exhibiting only minor variation.

Group 1 elements are correlative between key wells. High S, for example, is pervasive at the top, bottom, and two distinct intervals in the middle part of the A-1C. The relative abundances of Si, Al, and K also follow similar trends, with the highest values recorded in the top, middle, and bottom of the A-1C. While the signatures in Si, Al, and K are similar between wells, Dreves, Schultz, and Mutton have two times higher abundances of Si, Al, and K than the other wells.

Element	1σ (Photon counts)
Mg	870
Ca	2324
Al	121
Si	315
K	249
Fe	196
Co	21
Ti	11
Sr	67
S	55
Ni	17
Cu	25
V	80
Mo	39
Zn	17
Mn	20

Table 2: Elements reported with ED-XRF and their associated standard deviations (1σ) for 30 measurements.

Group 2 elements are not correlative between key wells. For example, there is no change in Ca, Mg, and V in the Dreves and David, but there is an apparent negative

correlation between Ca and Mg in the Bruske, KH 1054, St. Christensen, Schultz, and the Mutton, and a positive correlation between Mg and V in these six wells. The changes in Fe closely resemble those of Si, Al, and K in most wells, with high values in the middle and the bottom of the A-1C. However, Dreves and David exhibit anomalously high Fe in the middle and upper A-1C, respectively. The same is true for Sr, which closely resembles S except for anomalously high values in the lower A-1C in St. Christensen, Schultz, and Mutton, and overall lower abundances in Dreves and KH 1054. Ti and Zn show no temporal variation except for high values of Ti in the lower half of Bruske and David, and high values of Zn in the St. Christensen.

Group 3 elements are characterized by very little variation in key wells. These elements generally exhibit high frequency variation over a small range of values that near the standard error of the ED-XRF. Elemental trends observed in each well are described individually in figure captions.

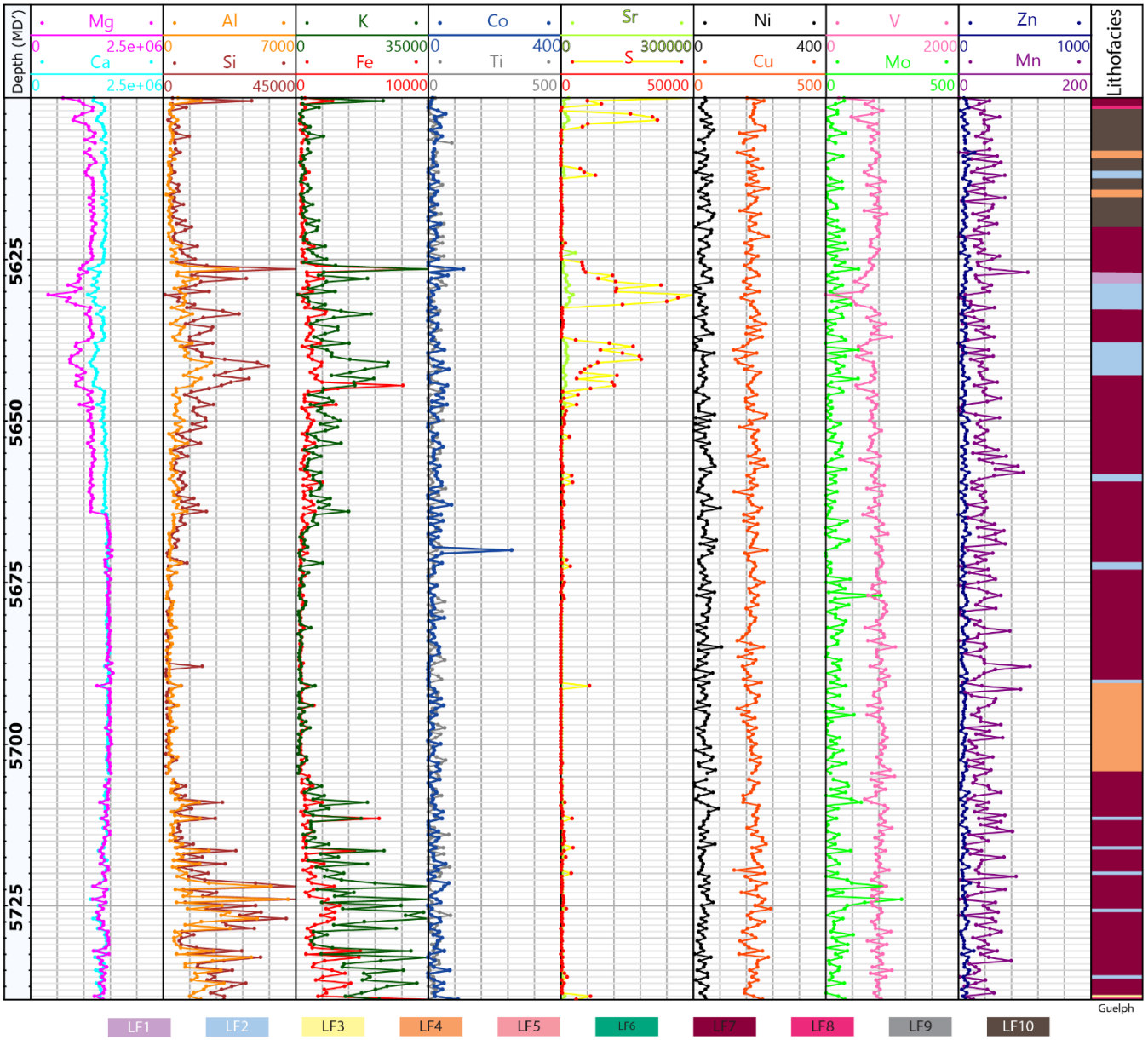

Figure 2: Elemental profile for the Dreves, Carl 1 well. Ca and Mg values are mostly unchanging, except for a slight decrease in Mg in the top half of the A-1C. Si, Al, K and Fe are relatively high at the top, middle, and base of the core, however Fe deviates from this trend with slightly lower values from 5645'-5635' and 5720'-5725'. Sr and S are highest at the top and upper section of the A-1C, with smaller highs at the bottom of the core. Ni, Cu, V, Mo, Mn, Ti and Co exhibit minor, high frequency variation with one large spike in Co at 5670'.

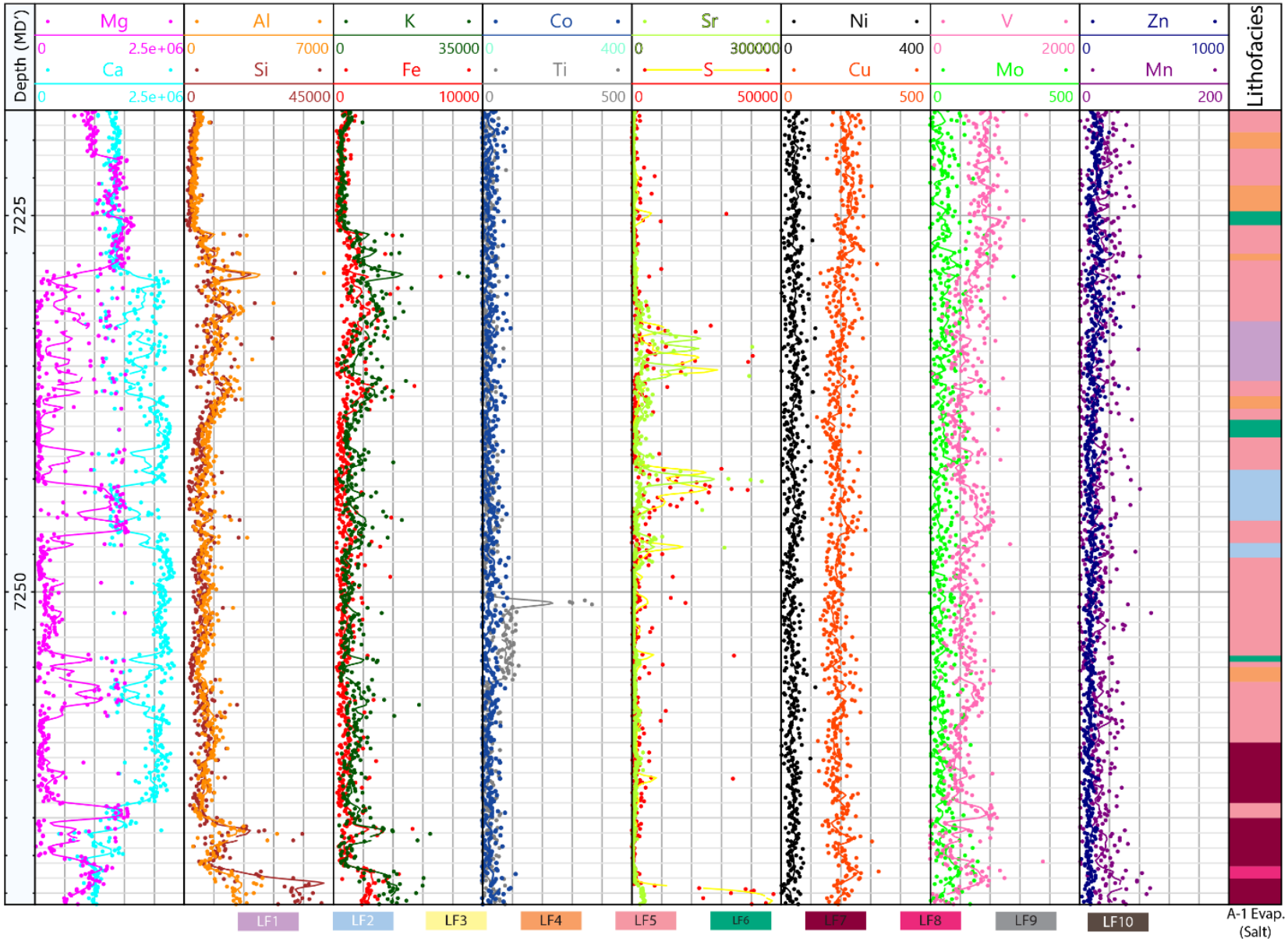

Figure 3: Elemental profile for the Bruske 1-26A well. Ca and Mg display an inverse relationship, while Mg and V covary for most of the core. Si, Al, K, and Fe are highest at the base and upper third of the core. Sr and S are highest in the middle and base of the core, with smaller spikes in the lower third of the A-1C. Ni, Cu, Mo, Mn, Ti and Co exhibit minor, high frequency variation with one large spike in Ti at 7252'-7270'.

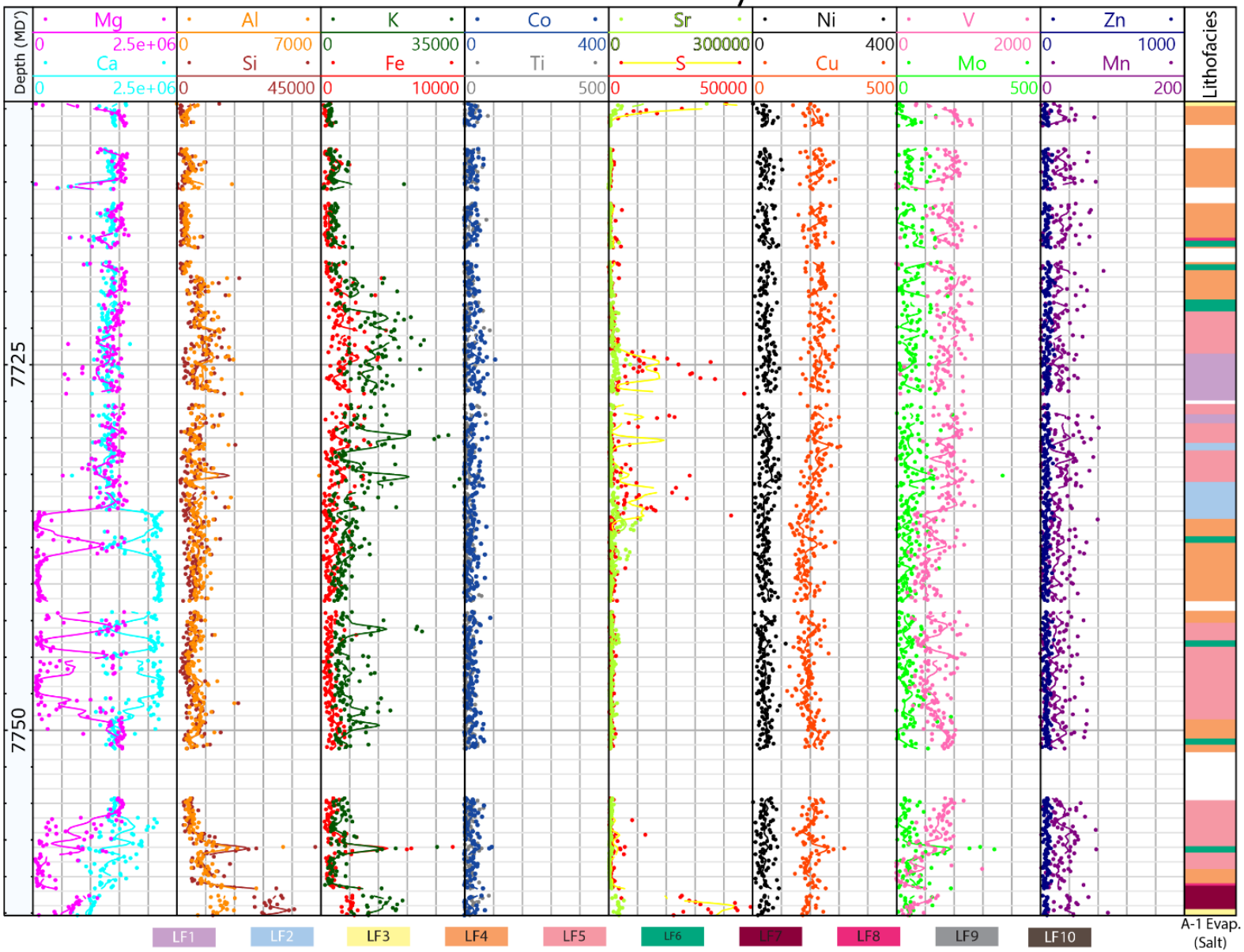

Figure 4: Elemental profile for the Kalium Hersey 1054 well. Ca, Mg, and V are relatively unchanged in the upper half of the core, with Ca and Mg displaying an inverse relationship, and Mg and V covarying. Si, Al, K, and Fe are highest at the base and upper third of the core, however K peaks are higher in respect to Si, Al, and Fe than in other wells. Sr and S are highest at the top, middle, and base of the core, with smaller spikes of these elements in the lower third of the A-1C. Ni, Cu, Mo, Mn, Ti and Co exhibit minor, high frequency variation with one large spike in Mo at 7740' and 7770'.

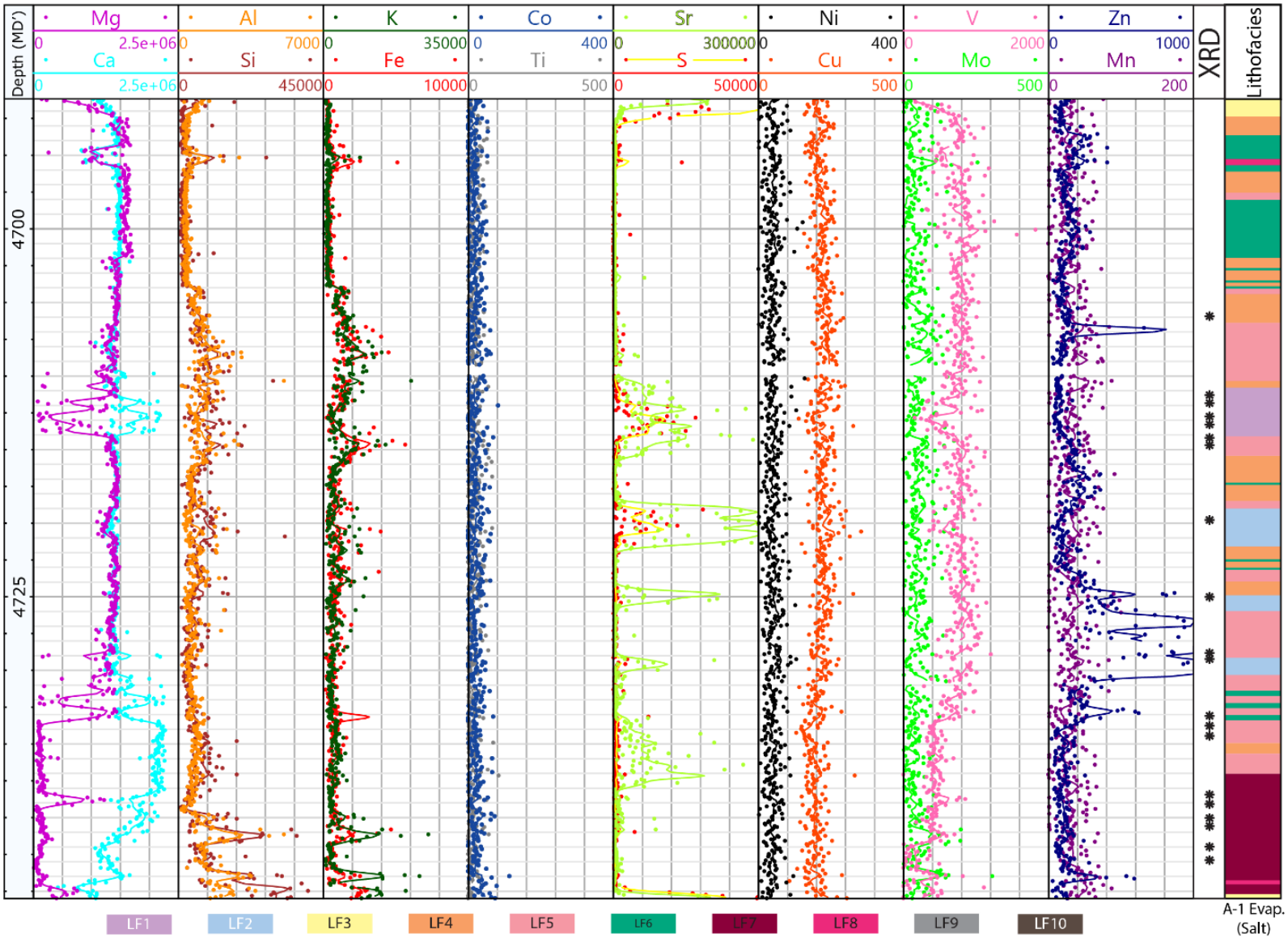

Figure 5: Elemental profile for the State Orange & Christensen 1-21P well. Ca, Mg, and V values are relatively unchanged in the upper three quarters of the core, except for low Mg and V from 4710'-4715' and 4733'-4745'. Si, Al, K and Fe are relatively high in the middle and base of the core, with one anomalous Fe spike at 4736'. Sr and S are highest at the top, middle, and base of the core, with anomalous high values in Sr from 4724'-4726' and 4733'-4738'. The highest Zn values recorded for these wells occurs from 4724'-4733' and another minor peak from 4706'-4708'. Ni, Cu, Mo, Mn, Ti and Co exhibit minor, high frequency variation throughout.

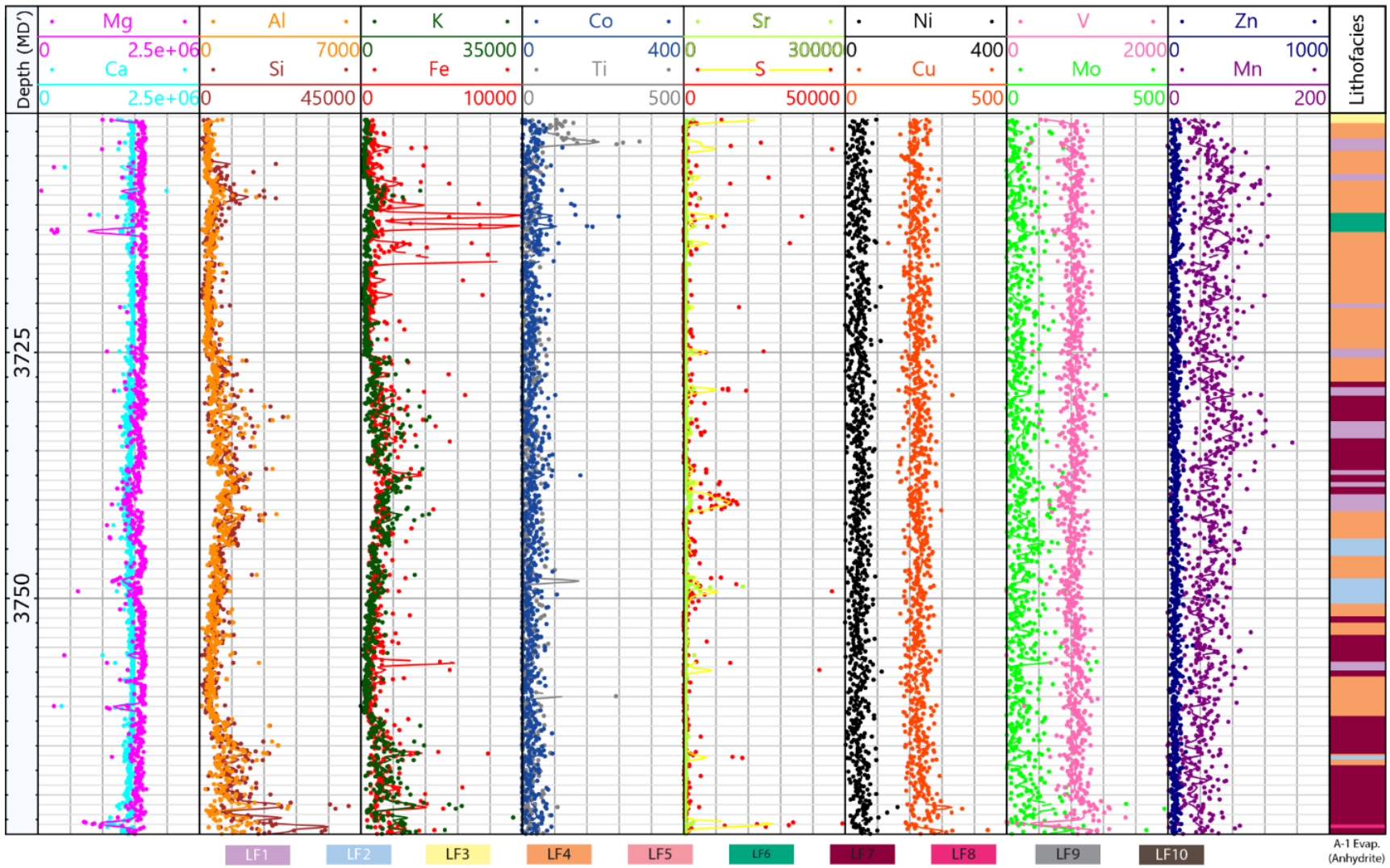

Figure 6: Elemental profile for the David, Donald L. 1 well. Ca, Mg, and V values are relatively unchanging throughout the A-1C. Si, Al, K, and Fe are relatively high in the middle and base of the core, with anomalous high Fe values from 3710'-3716' and 3756'-3758'. Sr and S are highest at the top and base, with multiple 1'-3' sections of high values throughout the A-1C. Ni, Cu, Mo, Mn, Ti and Co exhibit minor, high frequency variation.

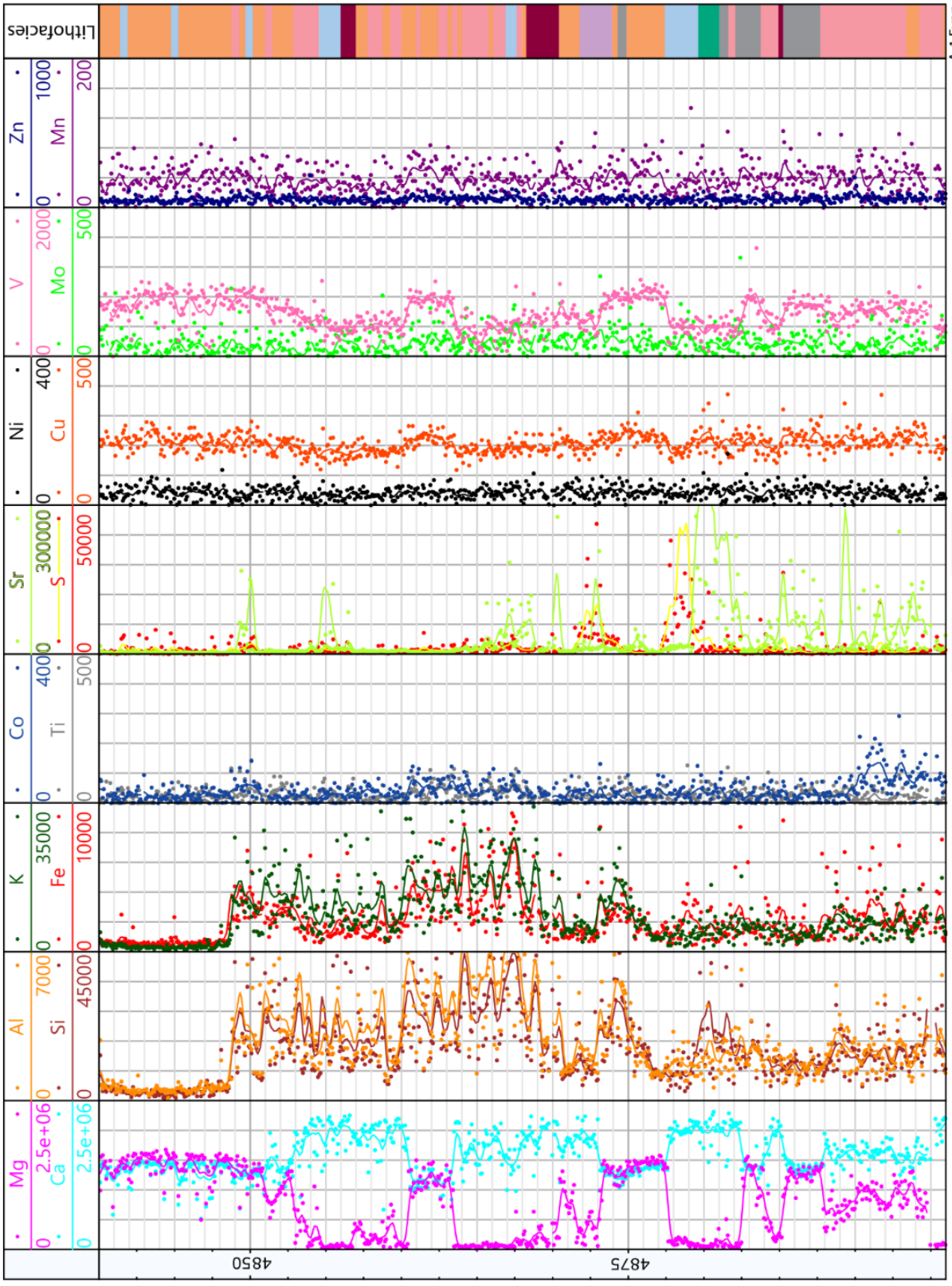

Figure 7: Elemental profile for the Schultz 1-36 well. Ca and Mg display an inverse relationship, while Mg and V covary for most of the core. Si, Al, K, and Fe are highest in the upper third of the core. Sr and S are highest in the lower third of the core, with the apparent covariation of S and Sr absent at the base of the A-1C. Ni, Cu, Mo, Mn, Ti and Co exhibit minor, high frequency variation throughout.

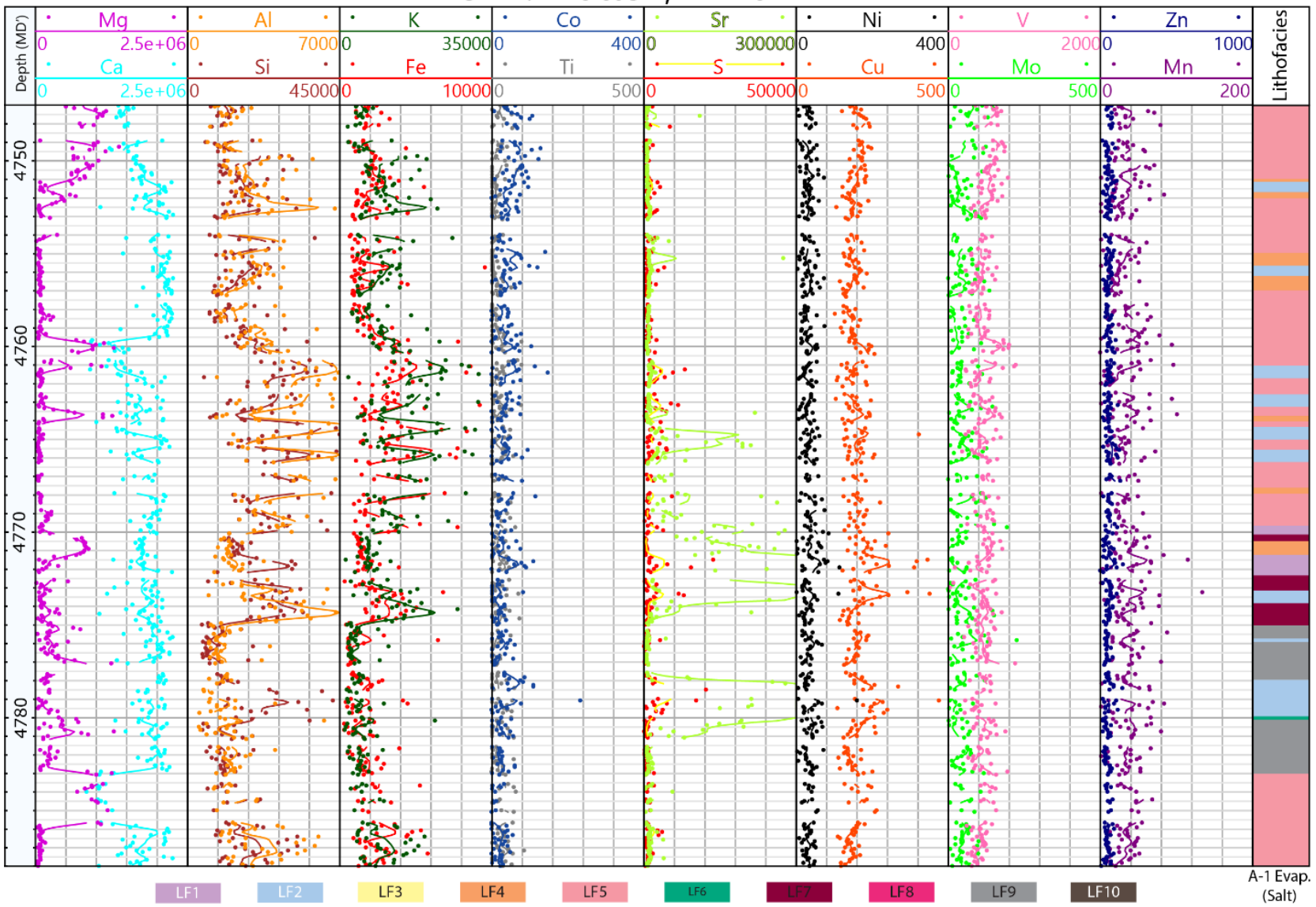

Figure 8: Elemental profile for the Mutton, William 1 well. Ca and Mg display an inverse relationship, while Mg and V covary for most of the core. Si, Al, K, and Fe are highest in the upper third of the core. Sr and S are highest in the lower third of the A-1C. Ni, Cu, Mo, Mn, Ti and Co exhibit minor, high frequency variation throughout.

	CLAYS				CARBONATES					OTHER MINERALS									TOTALS		
Depth (ft)	Chl	Kaol	Il/Mica	Mx I/S	Cal	Dol	Dol (Fe/Ca^{+})^{2}	Arag	Sid	Qz	K-spar	Plag	Py	Apa	Anhy	Ce	Ha	Ba	Clays	Carb.	Other
4706.30	Tr	Tr	Tr	Tr	1	97	0	0	Tr	1	Tr	1	0	0	0	0	0	0	Tr	98	2
4711.75	Tr	Tr	Tr	Tr	64	0	31	0	Tr	1	1	Tr	0	Tr	1	2	0	0	Tr	95	5
4712.40	Tr	Tr	Tr	Tr	6	0	79	0	Tr	1	1	1	0	0	6	6	0	0	Tr	85	15
4713.10	Tr	Tr	Tr	Tr	70	0	9	1	Tr	1	1	1	0	0	14	3	0	0	Tr	80	20
4713.85	Tr	Tr	Tr	Tr	18	55	0	0	Tr	1	1	1	0	0	19	5	0	0	Tr	73	27
4714.95	Tr	Tr	Tr	Tr	1	93	0	0	Tr	2	1	1	0	0	Tr	2	0	0	Tr	94	6
4720.65	Tr	Tr	Tr	Tr	1	97	0	0	Tr	1	Tr	Tr	Tr	0	1	0	0	0	Tr	98	2
4726.40	Tr	Tr	Tr	Tr	1	94	0	0	Tr	1	Tr	1	Tr	0	2	0	1	0	Tr	95	5
4729.75	Tr	Tr	Tr	Tr	3	90	0	0	Tr	1	Tr	Tr	Tr	0	6	0	0	0	Tr	93	7
4730.35	Tr	Tr	Tr	Tr	1	85	0	0	Tr	Tr	1	1	Tr	0	2	0	10	0	Tr	86	14
4734.25	Tr	Tr	Tr	Tr	86	10	0	0	Tr	Tr	Tr	Tr	1	0	0	3	0	0	Tr	96	4
4735.00	Tr	Tr	Tr	Tr	85	11	0	Tr	Tr	1	1	2	0	0	Tr	0	0	0	Tr	96	4
4735.95	Tr	Tr	Tr	Tr	73	23	0	0	Tr	1	1	Tr	Tr	0	Tr	1	1	0	Tr	96	4
4739.85	Tr	Tr	Tr	Tr	79	8	0	0	Tr	1	1	1	0	1	0	0	9	0	Tr	87	13
4740.50	Tr	Tr	1	Tr	61	14	0	Tr	Tr	1	Tr	1	0	Tr	0	0	22	0	1	75	24
4741.40	Tr	Tr	1	Tr	57	14	0	0	Tr	1	Tr	1	0	Tr	0	0	26	0	1	71	28
4742.05	Tr	Tr	1	Tr	46	10	0	0	Tr	1	1	Tr	Tr	Tr	1	0	40	0	1	56	43
4743.20	Tr	Tr	1	Tr	47	9	0	0	Tr	1	Tr	1	Tr	0	Tr	0	41	Tr	1	56	43
4744.55	Tr	Tr	1	Tr	28	14	0	0	Tr	1	1	1	Tr	0	Tr	0	54	0	1	42	57

Table 3: XRD results from St. Christensen. (Tr-Trace, Chl-Chlorite, Kaol-Kaolinite, Il/Mica-Illite/Mica, Mx I/S-Mixed layer illite/smectite, Cal-Calcite, Dol-Dolomite, Dol(Fe/Ca)^{2}-Ferroan Dolomite, Arag-Aragonite, Sid-Siderite, Qz-Quartz, K-spar-K-Feldspar, Plag-Plagioclase Feldspar, Py-Pyrite, Apa-Apatite, Anhy-Anhydrite, Ce-Celestine, Ha-Halite, Ba-Barite. Abbreviations modified from Ratcliffe et al. 2010).

Geochemistry and Mineralogy

Comparison of XRD results from St. Christensen with elemental cross-plots (Figure 10) and TOC measurements were used to establish mineralogical affinities and the relationship with organic carbon of elements measured with ED-XRF. Table 3 displays the abundances of minerals identified in St. Christensen with XRD.

Group 1 Element-Mineral Associations:

Based in the XRD results, there are several silicate minerals that are the likely source of Si, Al, and K measured with ED-XRF. Combined, these minerals make up less than 5 wt% of the bulk rock in St. Christensen, and include chlorite ($(Mg,Fe)_3(Si,Al)_4O_{10}(OH)_2 \cdot (Mg,Fe)_3(OH)_6$), kaolinite ($Al_2Si_2O_5(OH_4)$), illite-mica ($(K,H_3O)(Al,Mg,Fe)_2(Si,Al)_4O_{10}((OH)_2,(H_2O))$), mixed layer illite-smectite, quartz (SiO_2),

K-Feldspar ($KAlSi_3O_8$), and plagioclase feldspar ($Na(AlSi_3O_8) \leftrightarrow Ca(Al_2Si_2O_8)$). Figure 10A shows a positive relationship between Si, Al, and K, the 3 different trends likely representing the different elemental ratios in these siliciclastic minerals. Additionally, SEM was used to confirm the presence of silicate minerals in cored intervals with high Si, Al, and K (Figure 9; 4745.25' and 4708.5'). Samples from these intervals contained sparse, euhedral quartz crystals <50 µm in diameter and clay "booklets" >5 µm in diameter (Figure 9). EDS elemental maps indicate that the clay "booklets" are predominately composed of Si, Al, and K (Appendix 3).

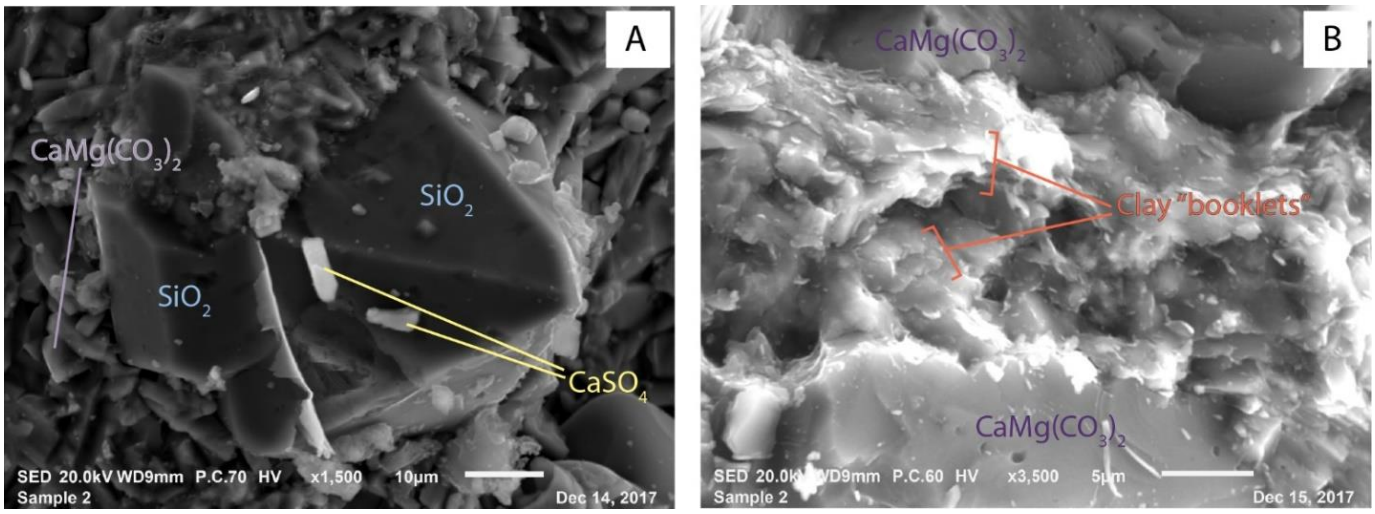

Figure 9: SEM photomicrographs from St. Christensen: A) Euhedral quartz crystal surrounded by a fine-crystalline dolomite matrix and minor anhydrite (Depth 4745.25'). B) A layer of clay "booklets" between dolomite crystals (Depth 4708.5').

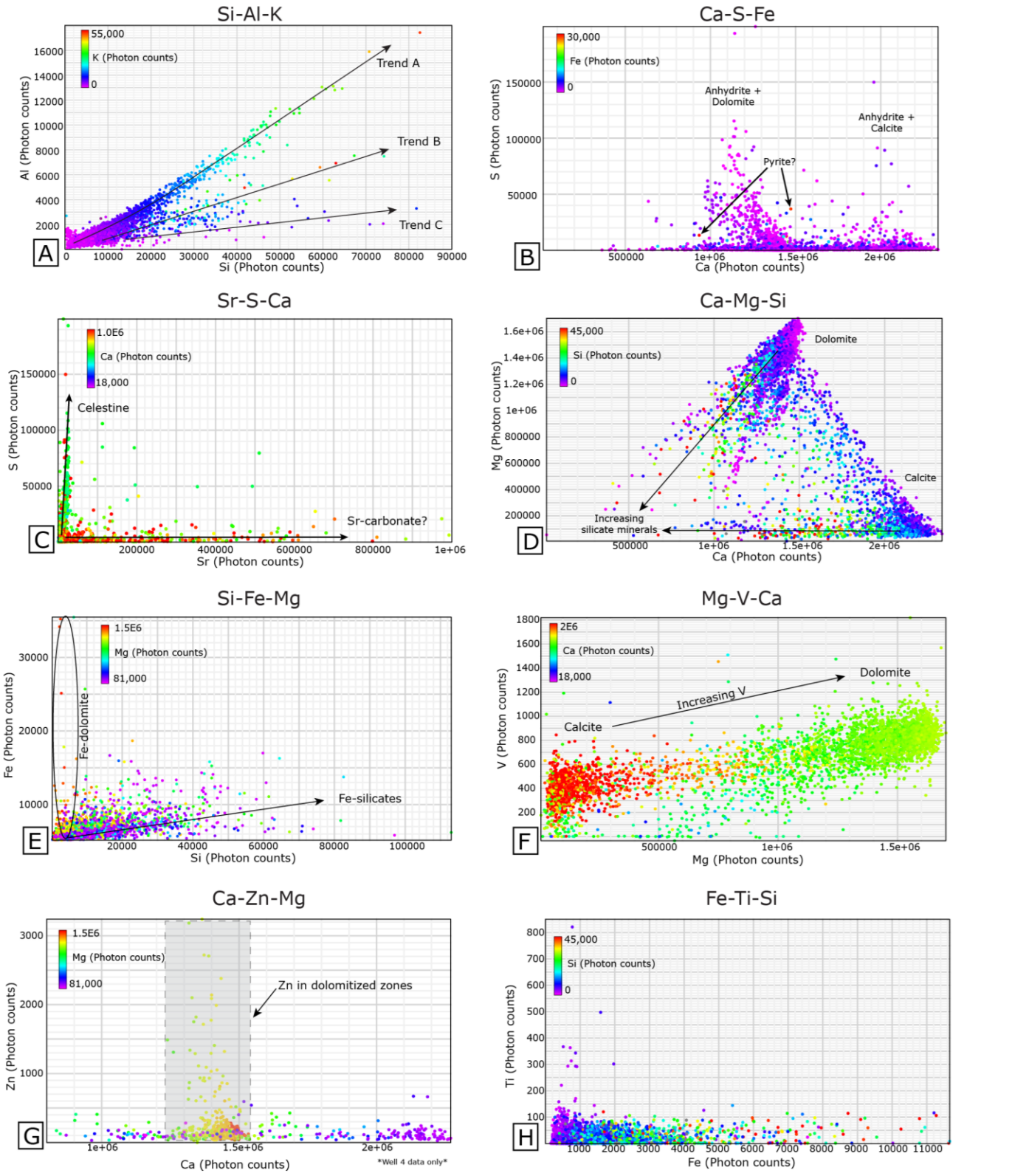

Figure 10: ED-XRF elemental cross-plots from all wells for A) Si-Al-K, B) Ca-S-Fe, C)Sr-S-Ca, D) Ca-Mg-Si, E) Si-Fe-Mg, F) Mg-V-Ca, G) Ca-Zn-Mg, and H) Fe-Ti-Si. In each plot, the first two elements listed are plotted on the x- and y-axis, and individual points are colored based on the abundance of the third listed element (scale in top right). Data for G) is only plotted for St. Christensen as this was the only well in the study to have significant variations in Zn.

XRD indicates that high S concentrations are likely associated with anhydrite ($CaSO_4$), celestine ($SrSO_4$), and pyrite (FeS_2) (Table 3). Calculated weight percent from XRD indicates that anhydrite is the dominant S-bearing mineral (0.1-19 wt%), followed by celestine (0.1-5 wt%), and pyrite (0.1-1 wt%). The multi-mineral association of S is evident in cross-plots between Ca-S-Fe, and Sr-S-Ca (Figure 10B and C). Figure 10B shows a bimodal distribution between Ca and S, with no systematic relationship with Fe. Because the two maxima in S are not associated with high Fe (Figure 10B), they likely represent anhydrite in a dolomite matrix and anhydrite in a calcite matrix. Figure 10C shows two trends between Sr and S: 1) high S:Sr, and 2) low S:Sr. The high S:Sr trend is interpreted to represent the presence of celestine. The mineral association of the low S:Sr trend is unknown since XRD results did not identify another Sr-bearing mineral in St. Christensen. However, the low S:Sr trend is associated with higher Ca values, an indication that Sr is linked to calcite in St. Christensen.

Group 2 Element-Mineral Associations:

Based on XRD results, calcite ($CaCO_3$) and dolomite ($CaMg(CO_3)_2$) are the dominant minerals (42-98 wt%) and therefore likely contribute the majority of Ca and Mg measured with ED-XRF (Table 3). Figure 10D shows that the relationship between Ca, Mg, and Si fall into 2 groups: 1) Ca-rich, and 2) Mg-rich. These two clusters likely represent calcite and dolomite, which was identified with XRD and reaction with acid during core description. Additionally, Figure 10D shows a decrease in Ca and Mg with an increase in Si, which likely reflects a shift from carbonate to silicate sedimentation.

XRD indicates there are six minerals that likely contribute to the Fe measured with ED-XRF: Ferroan dolomite ($Ca(Mg,Fe)(CO_3)_2$), pyrite, siderite ($FeCO_3$), chlorite,

illite-mica, and mixed illite-smectite (Table 3). Calculated weight percent from XRD indicate ferroan dolomite was only identified in two samples but with a concentration of 31-79 wt%, though pyrite, siderite, and Fe-silicates were found in the majority of samples ranging from 1 wt% to trace amounts. Figure 10E shows Si and Fe have a weak positive correlation, which is likely representative of chlorite, illite-mica, and mixed illite-smectite identified with XRD. High Fe and Mg associated with low Si is interpreted to reflect the presence of ferroan dolomite identified with XRD.

Though there is no V-bearing mineral reported in the XRD data (Table 3), Figure 10F suggests there is a positive relationship between Mg and V. A similar relationship exists between Zn and Mg in St. Christensen (Figure 10G). These observations suggest that V and Zn are associated with high Mg zones.

While there are no Ti-bearing minerals reported in the XRD data, numerous chemostratigraphic studies note the affinity of Ti to stable, heavy minerals including rutile/anatase (TiO_2), titanite ($CaTiOSiO_4$), titanomagnetite ($Fe^{2+}(Fe^{3+}, Ti)_2O_4$), and illmenite ($FeTiO_3$) (Craigie 2018 and the references therein). However, Figure 10H indicates there is no relationship between Ti and Fe or Ti and Si. While this does not rule out the possibility of Ti in rutile, without supporting XRD data the mineral association of Ti in the A-1C is unknown.

Group 3 Elemental Associations:

XRD results do not report any mineral sources for *Group 3* elements. Previous chemostratigraphic studies have demonstrated a relationship between elevated levels of *Group 3* elements, as well as V and Zn, with high TOC (Tribovillard et al. 2006, Algeo & Lyons 2006, Rowe et al. 2009, Dahl et al. 2013, Turner et al. 2016, Craigie 2018). V,

Zn, Co, Ni, Cu, Mo, and Mn were cross-plotted with TOC to examine this relationship. Figure 11 shows the distribution of TOC measured in Bruske, David, Schultz, Mutton, Dow, and Dalrymple. TOC ranges from 0.067 - 2.261 wt% organic carbon, with a mean value of 0.416 wt% and a median value of 0.379 wt%. Figure 12 shows cross-plots between Zn, V, Ni, Mo, Mn, Cu, and Co with TOC. For each of these elements there was no relationship between elemental abundance and wt% TOC, with an average R^2 of 0.007.

A summary of the element-mineral associations observed for *Group 1-3* elements are listed in Table 4.

Table 4: Summary of element-mineral associations identified from XRD and ED-XRF cross-plots.

Element	**Mineral Association** (Highest to lowest wt% from XRD)
Si	Quartz, plagioclase, K-feldspar, chlorite, kaolinite, illite-mica, mixed illite-smectite
Al	Plagioclase, K-feldspar, chlorite, kaolinite, illite-mica, mixed illite-smectite
K	K-feldspar, Illite-mica, mixed illite-smectite
S	Anhydrite, celestine, pyrite
Ca	Calcite, dolomite, aragonite, anhydrite, plagioclase, apatite
Mg	Dolomite, ferroan dolomite, chlorite, illite-mica, mixed illite-smectite
Fe	Ferroan dolomite, pyrite, siderite, chlorite, illite-mica, mixed illite-smectite
Sr	Celestine, Sr-carbonate?
V, Zn	Associated with dolomite
Ti, Ni, Mo, Mn, Cu, Co	Unknown

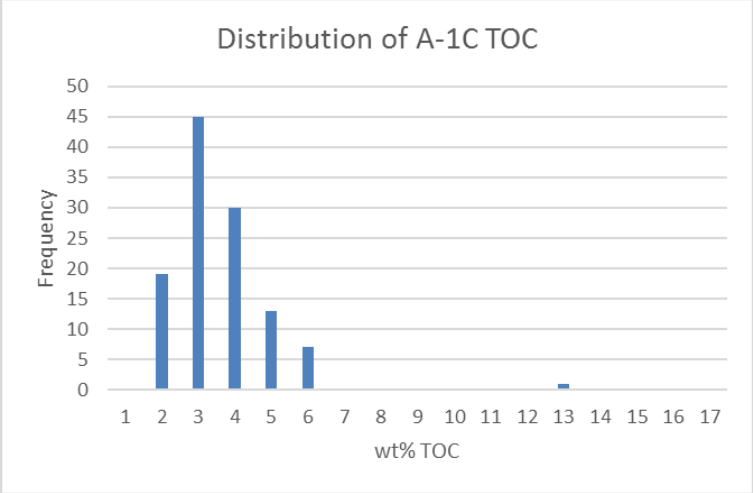

Figure 11: Histogram of wt% TOC in the A-1C from Bruske, David, Schultz, Mutton, Dow, and Dalrymple

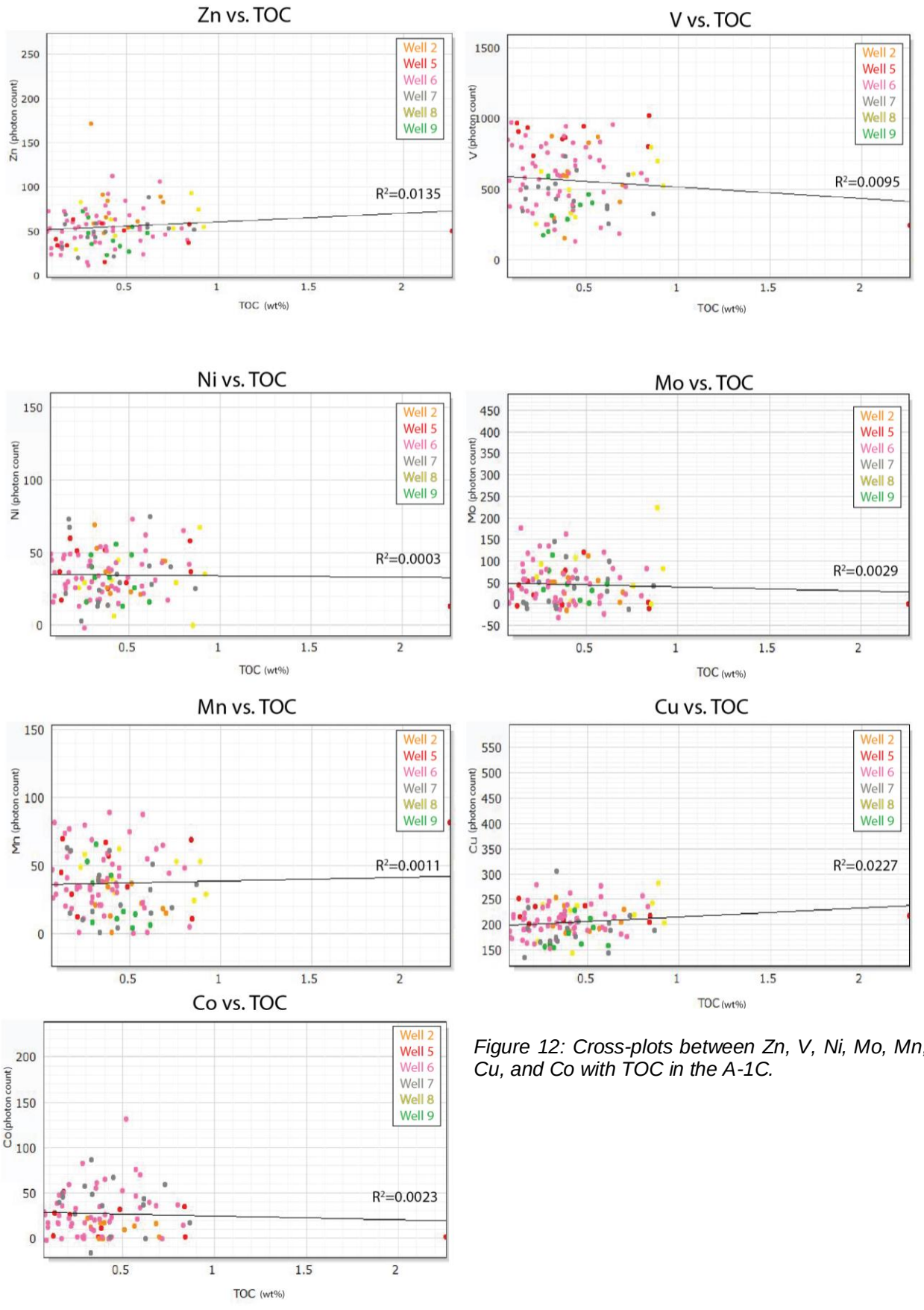

Figure 12: Cross-plots between Zn, V, Ni, Mo, Mn, Cu, and Co with TOC in the A-1C.

Lithofacies Analysis

Cores from key wells were examined to identify lithofacies and sedimentary structures and textures. Figure 13 displays 10 lithofacies identified in core and Figures 2-8 compares these lithofacies with elemental data.

Lithofacies fall into 4 groups: mixed mudstone-anhydrite (*LF1-LF3*), mudstone dominant (*LF4-LF7*), rudstone (*LF8*), and mixed mudstone-wackestone (*LF9-LF10*). These lithofacies are consistent with lithofacies identified in previous A-1C studies (Gill 1973, Budros 1975, Budros & Briggs 1977, and Rine et al. 2017). Bruske, KH 1054, and St. Christensen are composed primarily of mudstone-dominant lithofacies, while Dreves, David, Schultz, and Mutton are majority mudstone with minor wackestone lithofacies. Wavy laminated mudstone with sparse algal mats (*LF10*) is only observed in the upper 15 ft of Dreves. In all wells, the A-1C is bifurcated by anhydrite lithofacies (*LF1 and LF2*), which Rine et al. (2017) identifies as the basin center equivalent of the "Rabbit Ears Anhydrite" identified in previous studies. Laminated anhydrite lithofacies (*LF3*) are observed at the contacts between the A-1C and the underlying A-1 Evaporite in Bruske, KH 1054, St. Christensen, and David and at the overlying contact with the A-2 Evaporite in Dreves, KH 1054, St. Christensen, and David. Rudstone lithofacies (*LF8)* composed of angular clasts of laminated mudstone occurs in Bruske, KH 1054, St. Christensen and David, ~1 ft from the base of the A-1C and has a sharp contact with underlying lithofacies.

In additional to identifying A-1C lithofacies, the relationship with the overlying and underlying formations was noted in each well. Bruske, KH 1054, St. Christensen, Schultz, and Mutton overly the salt lithofacies of the A-1 Evaporite, David overlies

anhydrite lithofacies of the A-1 Evaporite, and Dreves overlies Guelph lithofacies divided by a rip-up clast rudstone (*LF8)*. Overlying the A-1C in Bruske, KH 1054, St. Christensen, Schultz, and Mutton is the salt lithofacies of the A-2 Evaporite, and anhydrite lithofacies of the A-2 Evaporite in Dreves and David.

As observed in other chemostratigraphic studies, ED-XRF data show that the majority of elemental variation cannot be visually observed within individual lithofacies. For example, Figure 14 shows a decrease in Si, Al, and K upward through a texturally homogeneous interval. This observation is used as further rationale for why ED-XRF was used to characterize A-1C mudstones.

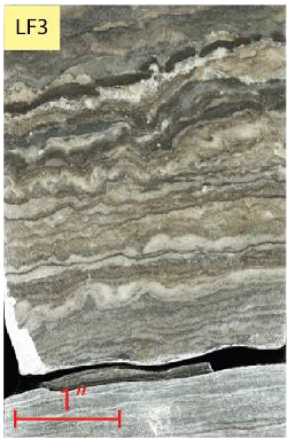

LF1	Nodular anhydrite in a gray to black, thinly laminated (0.5-1 cm) dolomite mudstone. Nodules are ~0.25-1 cm in diameter and surrounded by black, insoluable residue.
LF2	Laminated anhydrite in a gray to black, thinly laminated (0.5-1 cm) dolomite mudstone. Anhydrite appears as cement, sparse nodules <5 mm in diameter, and clusters of <1mm crystal laths.
LF3	Brown to tan, crinkly laminated anhydrite (1-2 cm thick) with thin laminations (0.5-1 cm thick) of dolomite mudstone.
LF4	Dark black dolomite mudstone. Relatively masssive beds (1-2 ft thick) and lacks any apparent sedimentary textures or structures.
LF5	Dark black dolomite mudstone with fine (<1 mm thick), wavy laminations. Partings have concentrated organic matter, sparse pellets, insoluable residue. "Poker chip" facies from previous studies.
LF6	Dark black , heavily fractured dolomite mudstone. Vertical fractures filled with white saddle dolomite, anhydrite, and halite. Underlying mudstone fabric varies from massive to finely laminated.
LF7	Brown to tan, laminated (1-5 mm thick) mixed dolomite and calcite mudstone. Coarser-grained material, likely quartz and other lithics, concentrated along laminations.
LF8	Brown to tan laminated rudstone. Overturned and fragmented clasts of laminated mudstone ranging from 1-5 cm in diameter.
LF9	Brown to gray dolomitic mudstone with flecks and thin lenses of organic matter, insoluable residue, pyrite, and sparse pellets. Bedding ranges from 2-10 cm.
LF10	Brown to tan dolomitic mudstone with thin wavy laminations and algal mats. Dolomitization has often severely altered the primary fabric.

Figure 13:Lithofacies descriptions and photographs

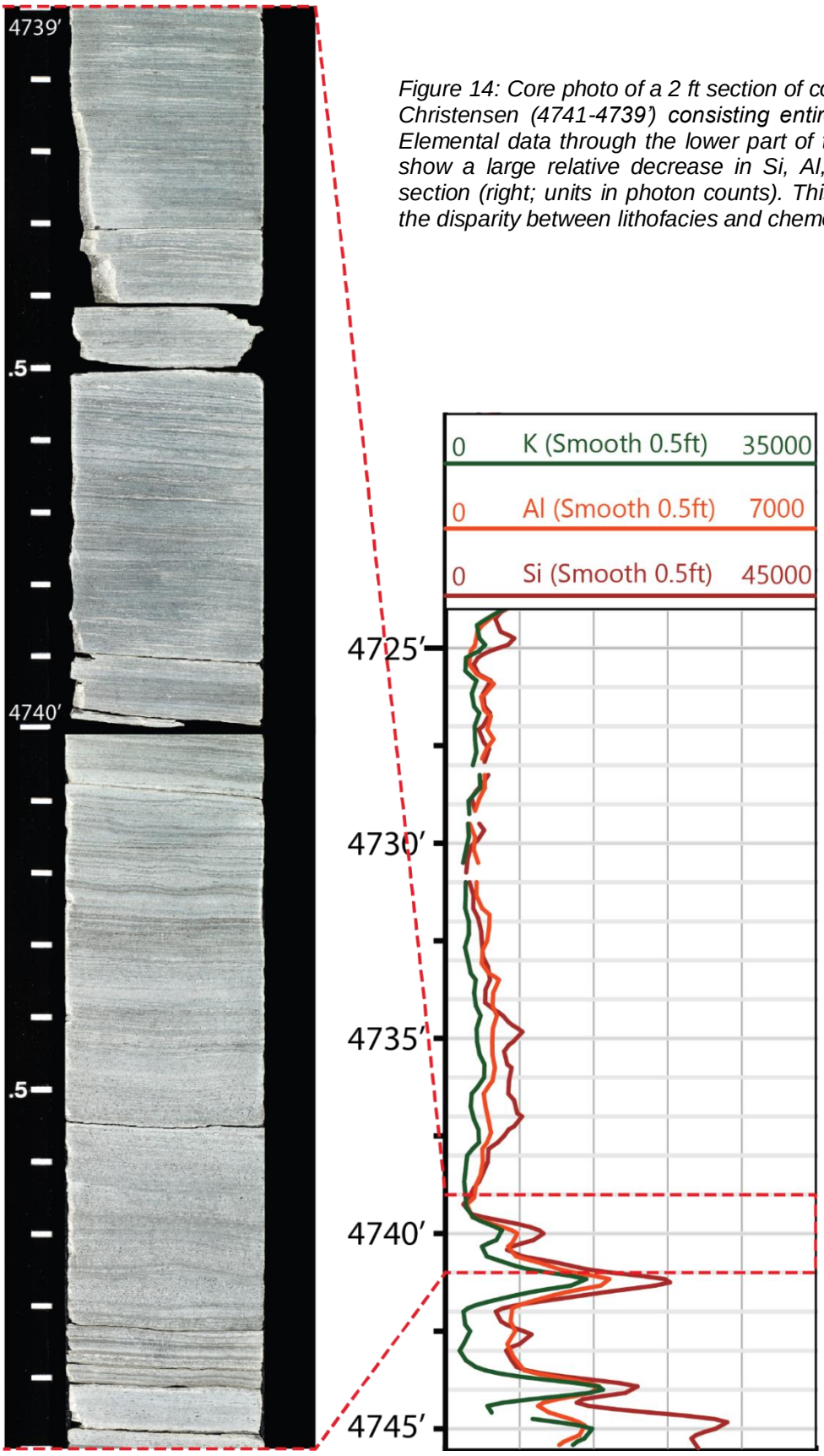

Figure 14: Core photo of a 2 ft section of core from St. Christensen (4741-4739') consisting entirely of LF7. Elemental data through the lower part of this interval show a large relative decrease in Si, Al, and K up section (right; units in photon counts). This highlights the disparity between lithofacies and chemofacies

PCA-derived Chemofacies

PCA analysis was used to statistically assign chemofacies using Group 1 elements for correlation in key wells. Previous chemostratigraphic studies noted the importance of separating different lithologies for correlation to diminish the masking effect that gross lithological shifts have on subtle elemental changes (Pearce et al. 2005, Ratcliffe et al. 2006, 2015, and Hildred et al. 2010). Therefore, Si, Al and K where analyzed separately from S, and high S zones were not considered for Si, Al, and K PCA chemofacies. Additionally, this study does not use PCA in the traditional method to identify element-mineral associations, instead only used PCA to statistically define chemofacies groups after elemental-mineral associations were examined with XRD and elemental cross-plots

Figure 15 displays PCA results for S in St. Christensen, run with 2, 3, 4 and 5 clusters and Table 5 displays the average distance ratio (*s(i)*) for each PCA run. Clusters were divided into high and low S values, and the addition of more clusters further subdivided chemofacies on this basis. PCA with 2 clusters has the highest average *s(i)*=0.888, followed by 3 clusters *s(i)*=0.886, 4 clusters *s(i)*=0.874, and 5 clusters *s(i)*=0.746. However, PCA using 2-4 clusters do not recognize smaller increases in S that are identified with 5 cluster PCA (depths 4729-4741 ft). Additionally, each of these runs have a relatively high *s(i),* therefore PCA with 5 clusters will be used to designate S-chemofacies (SFC) in the remaining wells.

Table 5: Average distance ratio (s(i)) for 2, 3, 4, and 5 cluster PCA for Si, Al, K, and S chemofacies

	2 Clusters	3 Clusters	4 Clusters	5 Clusters
PCA for S Chemofacies	**avg *s(i)* = 0.888**	**avg *s(i)* = 0.886**	**avg *s(i)* = 0.874**	**avg *s(i)* = 0.746**
PCA for Si, Al, K Chemofacies	**avg *s(i)* = 0.68**	**avg *s(i)* = 0.53**	**avg *s(i)* = 0.50**	**avg *s(i)* = 0.45**

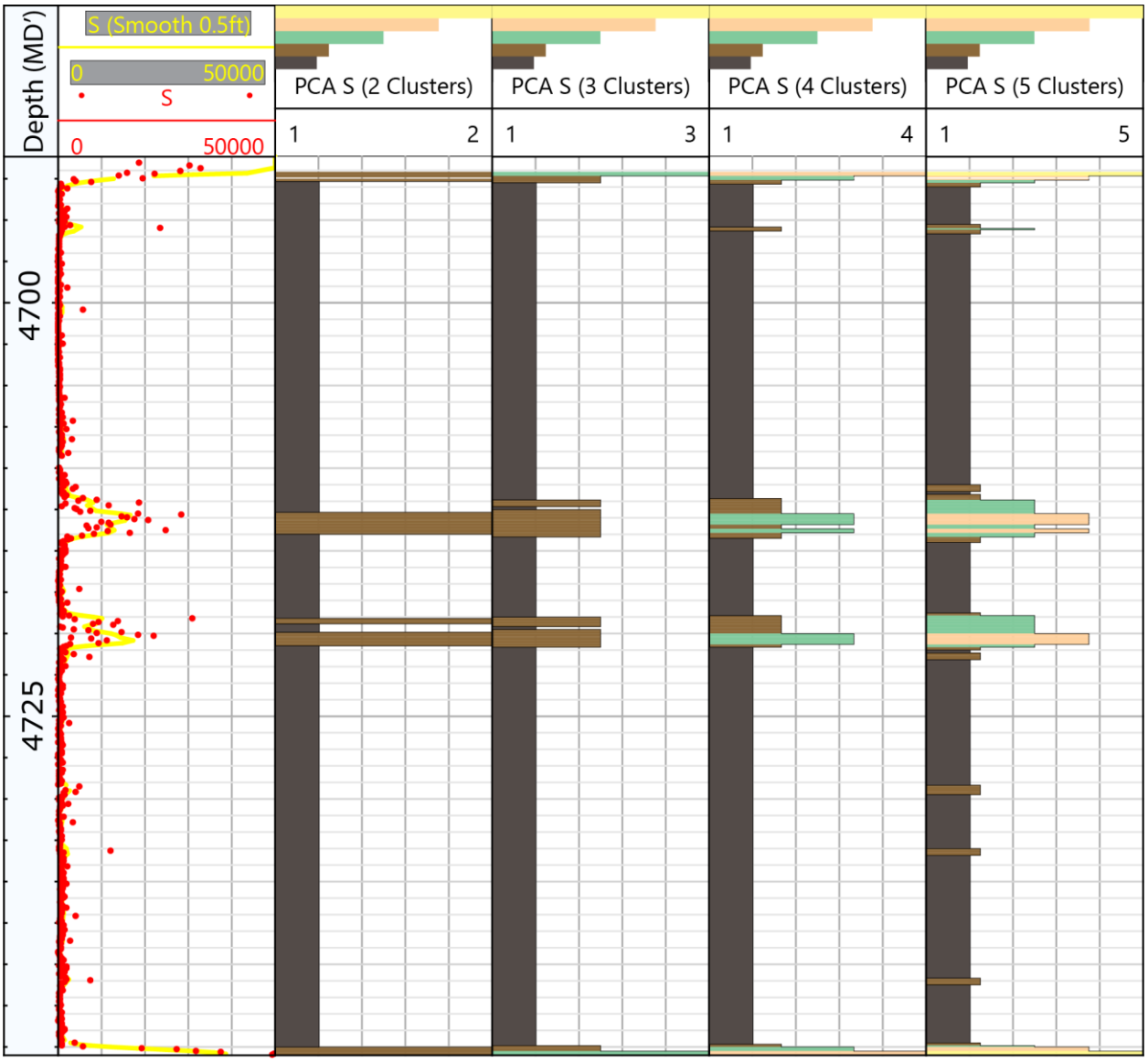

Figure 15: Profile of St. Christensen showing S-Sr PCA results for 2, 3, 4, and 5 clusters.

Figure 16 shows Si, Al, and K PCA results with 2, 3, 4 and 5 clusters, and Table 5 displays the average distance ratio (*s(i)*) for each PCA run. Si, Al, and K clusters were constructed based on the relative abundances of these elements, with high abundances grouped in separate clusters than low abundances. Comparison of these different input parameters shows decrease in distance ratio from 2 to 5 clusters (0.68 – 0.45). Based on this metric, 2 clusters is the statistically ideal parameter for defining chemofacies for

Si, Al, and K. However, visual inspection of clusters between the four runs shows that the 5 cluster PCA captures variation that is lumped together in analyses with fewer clusters (Figure 16; depths 4700'-4709'). By adding more clusters to the PCA, the range of Si, Al, and K values is incrementally subdivided but the relationship between clusters remains the same. Therefore, PCA with 5 clusters will be used to designate Si, Al, K-chemofacies (SAK-CF) in the remaining wells for siliciclastic minerals.

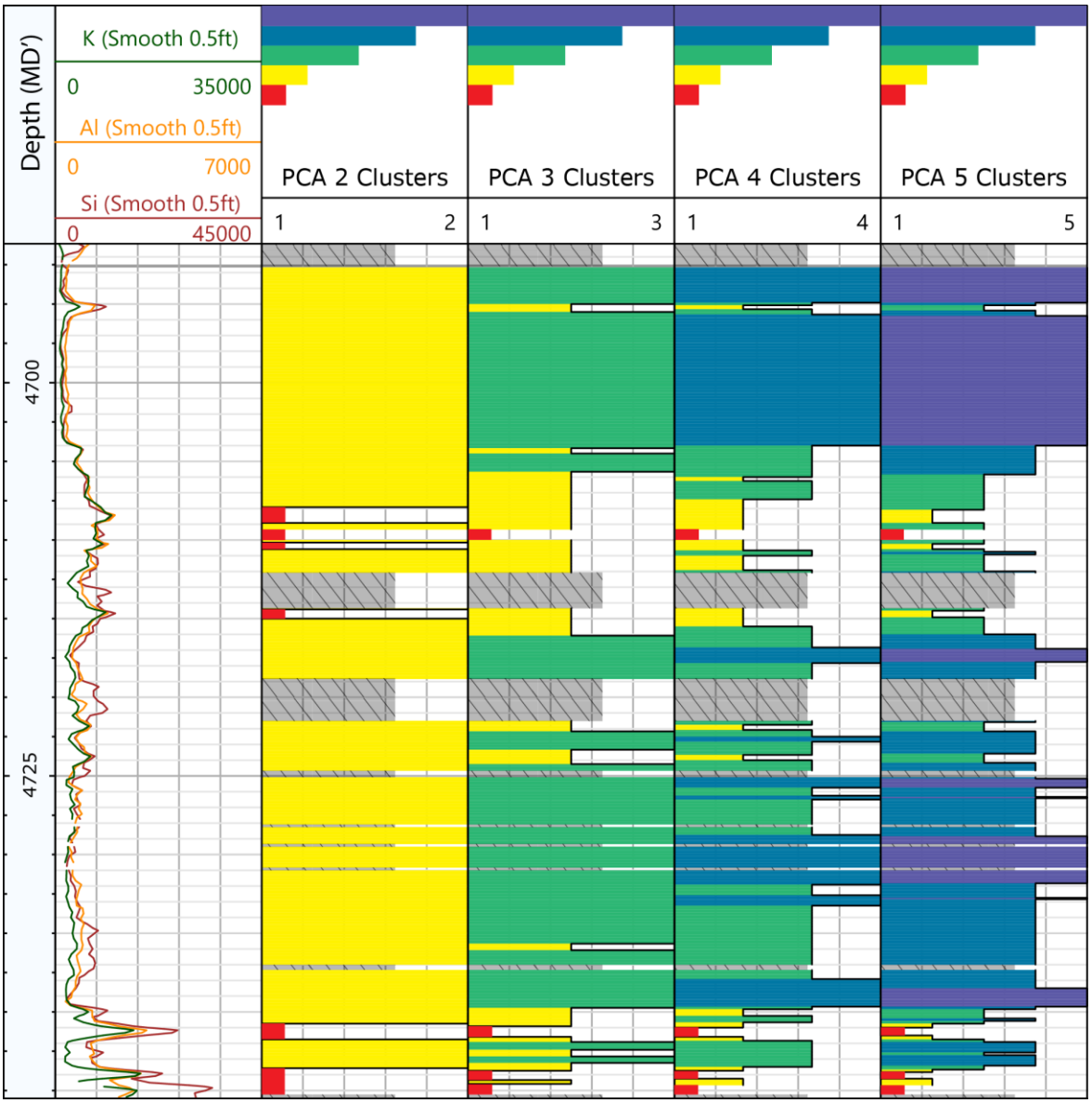

Figure 16: Profile of St. Christensen displaying Si-Al-K PCA results for 2, 3, 4, and 5 clusters.

Chemofacies Correlation

PCA chemofacies were used to guide the correlation of elemental signatures from margin to basin center for both the northern (Figure 18, A-A') and southern slope (Figure 19, B-B'), which are shown in Figure 17. Elemental correlations were further constrained stratigraphically by erosional surfaces identified in core (*LF8)*. Stratigraphically, Si, Al, and K exhibit a cyclic pattern of steady, gradational increases followed by an abrupt decrease (Figure 18 and 19). The relative maxima at Si, Al, K-cycle tops (SAK-cycles) were correlated between key wells. Fourteen SAK-cycle tops (*SAK1-SAK14*) were identified in Bruske, KH 1054, St. Christensen, and David (Figure 18 and 19). Thirteen of the fourteen SAK-cycles (*SAK2-SAK14*) were identified in Dreves, with the lower most cycle unrecognized. In Schultz and Mutton, cycles *SAK5-SAK11* and *SAK8-SAK10* were identified, respectively. These upper and lower most SAK-cycles were not recognized to Schultz and Mutton as these wells did not core the bottom and top of the A-1C.

Sulfur also displays repetitive trends characterized by consistently low abundances punctuated by sharp increases that are a symmetric "bell-shape". S zones fall into three types (*Type I, II, and III)* based on correlation patterns and extent. Four, regionally high S zones (Figures 18 and 19, *Type I* S zones *A, B, C*, and *D*) were identified in all key wells. *Type I* zones *A* and *D* are present at the base and top of the A-1C, respectively, while *Type I* zones *B* and C bifurcate the A-1C. Figures 18 and 19 show that *B* and *C* are regionally correlative in all seven key wells, but *A* is absent in Dreves. Additionally, smaller S increases, depicted as the light blue *Type II* zones in Figures 18 and 19, are locally correlative between adjacent wells. Bruske, KH 1054, and

St. Christensen have fewer than four *Type II* S zones while Dreves, David, Schultz, and Mutton contain between 6 and 9 *Type II* zones. Finally, the majority of wells contain several high S intervals associated with fractured bedding and coarse crystalline anhydrite (*Type III* S zones, colored pink in Figures 18 and 19). *Type III* S zones are non-correlative between adjacent wells.

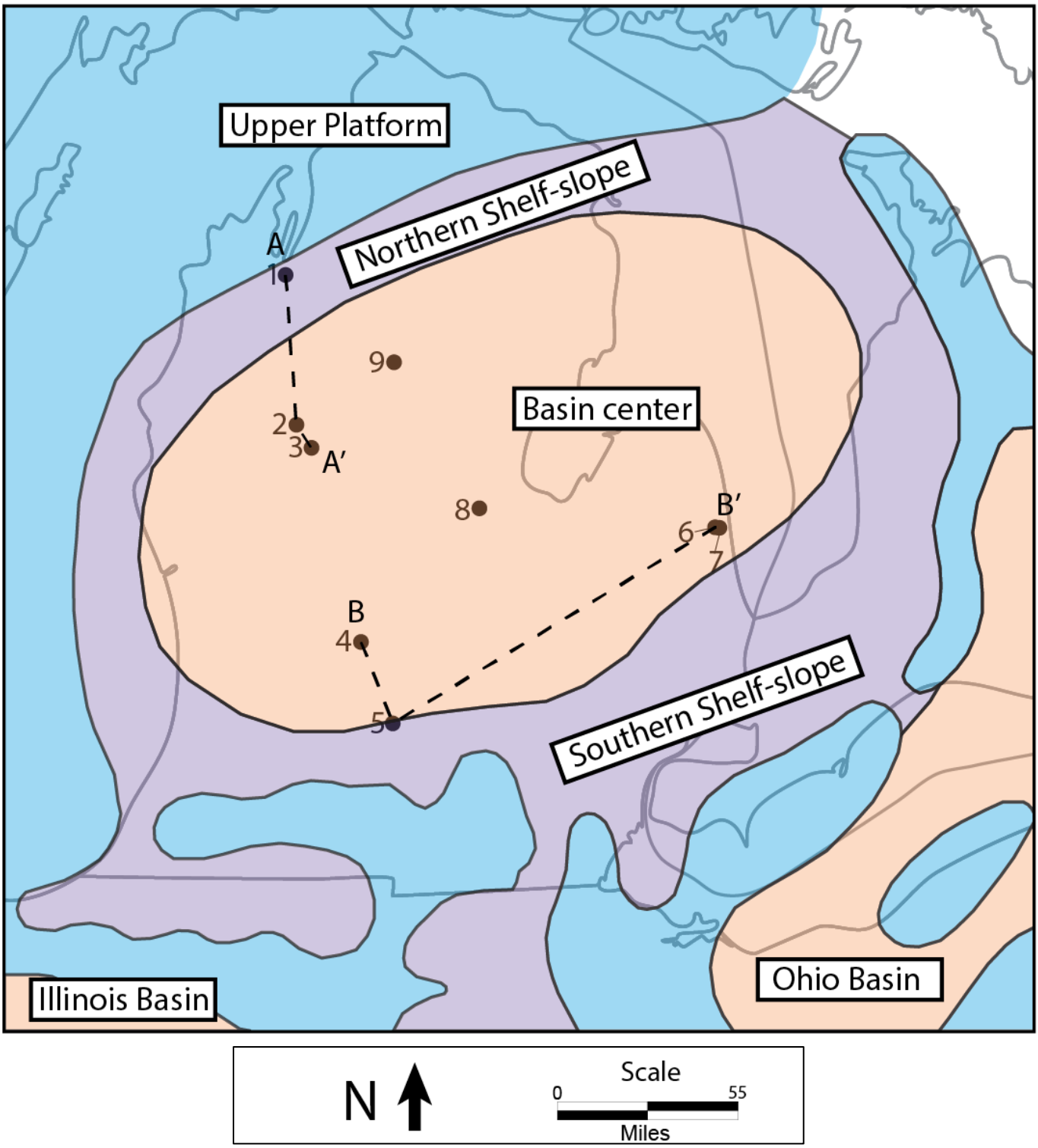

Figure 17: Map displaying northern (A-A') and southern (B-B') transects. (Modified from Rine et al. 2017)

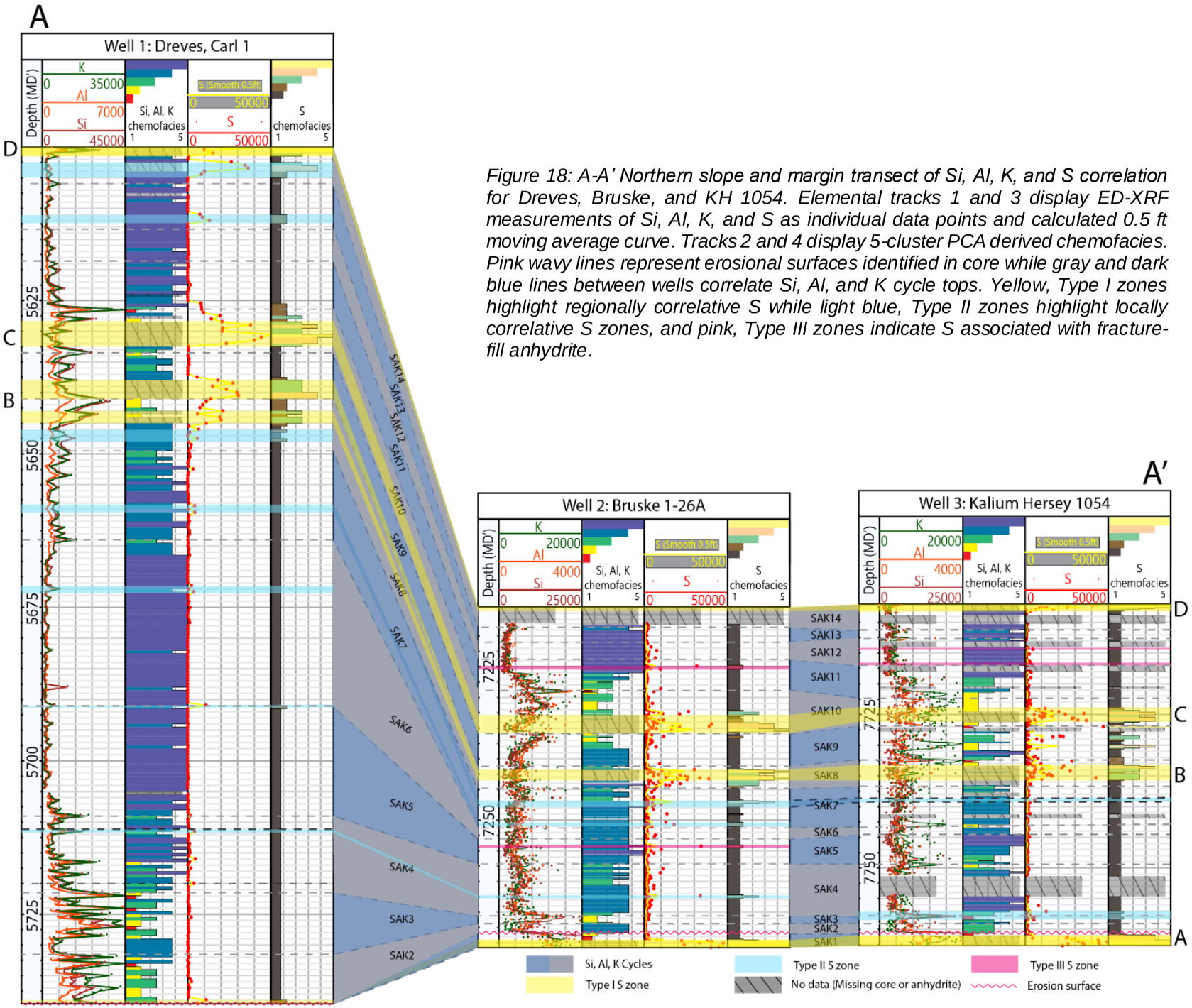

Figure 18: A-A' Northern slope and margin transect of Si, Al, K, and S correlation for Dreves, Bruske, and KH 1054. Elemental tracks 1 and 3 display ED-XRF measurements of Si, Al, K, and S as individual data points and calculated 0.5 ft moving average curve. Tracks 2 and 4 display 5-cluster PCA derived chemofacies. Pink wavy lines represent erosional surfaces identified in core while gray and dark blue lines between wells correlate Si, Al, and K cycle tops. Yellow, Type I zones highlight regionally correlative S while light blue, Type II zones highlight locally correlative S zones, and pink, Type III zones indicate S associated with fracture-fill anhydrite.

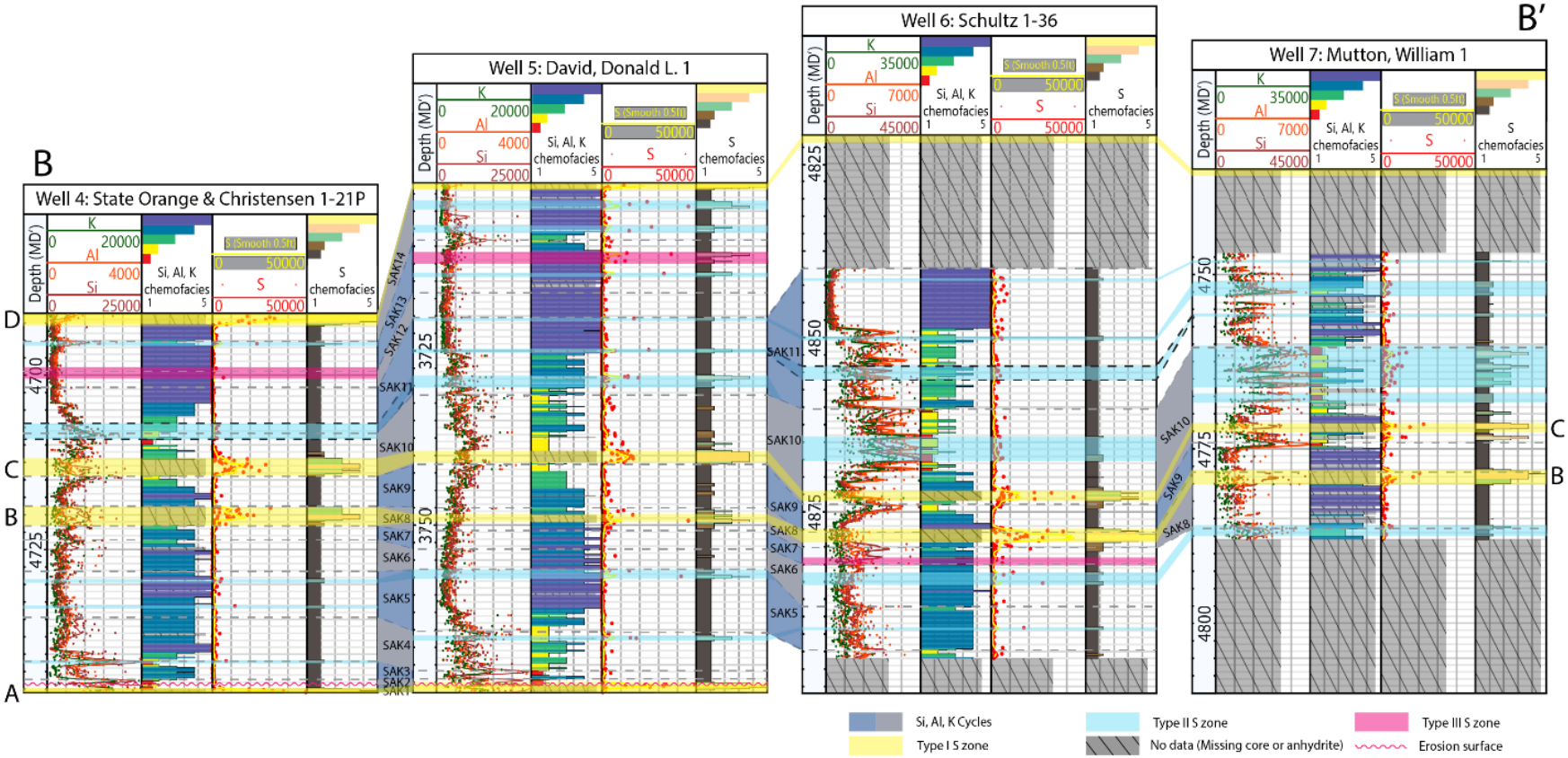

Figure 19: B-B' Southern slope and margin transect of Si, Al, K, and S correlation for St. Christensen, David, Schultz, and Mutton. Elemental tracks 1 and 3 display ED-XRF measurements of Si, Al, K, and S as individual data points and calculated 0.5 ft moving average curve. Tracks 2 and 4 display 5-cluster PCA derived chemofacies. Pink wavy lines represent erosional surfaces identified in core while gray and dark blue lines between wells correlate Si, Al, and K cycle tops. Yellow, Type I zones highlight regionally correlative high S while light blue, Type II zones highlight locally correlative S zones, and pink, Type III zones indicate S associated with fracture-fill anhydrite.

DISCUSSION

Genetic Relationship of Elemental Signatures

The ability to correlate SAK-cycles and *Type I* S zones across the Michigan Basin (Figures 18 and 19) supports the hypothesis that texturally homogeneous A-1C basin-center mudstones have spatially correlative elemental signatures (i.e. chemofacies). Widespread correlation of SAK-CF cycles and *Type I* S zones *A-D* further indicates that spatial and temporal variations in Si, Al, K, and S signatures were controlled by consistent large-scale changes. However, *Type II and III* S zones are not regionally correlative, indicating these S zones do not share the same basin-wide controls as *Type I* S zones A-D. Additionally, not all elements measured in this study display correlative trends. For example, Mg, Ca, Fe, V, Sr, and Zn display distinct temporal variation but lack spatially correlative trends. Other elements, such as Co, Ti, Ni, Cu, Mo, and Mn, lack any distinct temporal variation altogether.

The second hypothesis that elemental variations reflect temporal changes in relative sea-level, redox conditions, and sedimentation rate follows from the first hypothesis. To evaluate the second hypothesis, element variability must be determined in the context of primary deposition or secondary alteration. The degree of spatial correlation on a basin-wide scale, or lack thereof, provides an indication about whether the geochemical signal represents primary deposition or diagenetic alteration. The degree of spatial correlation along with core observation, minerology from XRD and elemental cross-plots were used to interpret the genetic relation of elemental signals.

The observed Si, Al, and K variability is interpreted to reflect temporal variations in primary clastic sedimentation. Evidence that Si, Al, and K represent variations in

clastic deposition includes the presence of silicate minerals identified with XRD and the positive relationship between these three elements in cross-plots (Table 3 and Figure 10A). Evidence that these elements represent primary deposition includes spatial correlativity across the basin and the lack of a relationship with dolomitized zones, indicating the diagenetic fluids responsible for dolomitization likely did not influence Si, Al, and K elemental signatures (Figure 2-8).

Intervals exhibiting high abundances of S are interpreted to reflect the presence of anhydrite, which is interpreted to have formed by either: (i) diagenetic alteration of primary gypsum, and/or (ii) secondary precipitation of anhydrite associated with burial or hydrothermal fluids. The interpretation that S variations reflect changes in the abundance of anhydrite is supported by the observation that anhydrite lithofacies are recognized in core, and XRD data indicating anhydrite as the most abundant S-bearing mineral in these intervals. Importantly, Figure 10B shows that high S intervals do not correlate with high Fe, evidence that S trends do not reflect the abundance of pyrite. Anhydrite associated with *Type I* S zones A-D (Figure 18 and 19, yellow zones) is interpreted as primary gypsum deposition based on its basin-wide occurrence and preserved primary bedding textures observed in core. *Type II* S zones in Figures 18 and 19 are interpreted to originate from primary gypsum deposition caused by locally restricted sea water chemistry in shallow, restricted environments. *Type III* S zones that are not correlative between adjacent wells, observed in Bruske, KH 1054, St. Christensen, David, and Schultz in Figures 18 and 19, are associated with fractured intervals and are interpreted to reflect mineralization by fault-related hydrothermal fluids.

Variability in Ca and Mg is interpreted to reflect two processes: (i) primary aragonite and calcite deposition represented by high Ca, and (ii) dolomitization of primary limestone represented by high Mg. XRD-determined mineralogy and the Ca-Mg relationship in Figure 10D are evidence that intervals with high Ca:Mg represent calcite, while low Ca:Mg represents dolomite. The lack of spatial correlation in Ca and Mg trends, especially between adjacent wells, is evidence that the observed Ca:Mg likely does not reflect the ratio of these elements at the time of deposition. Additionally, fractured lithofacies observed in core containing “saddle” dolomite suggest that hydrothermal fluids played in a role in dolomitization. Figure 10F shows that high V and Mg are positively correlated, implying that high V is associated with dolomitization in the A-1C. To the author’s knowledge, there are no previous studies that recognize V associated with dolomite, and further investigation is needed to understand this association.

Temporal variation in Fe is interpreted to reflect changing abundances of multiple Fe-bearing minerals that represent primary deposition and diagenetic alteration. XRD indicated the presence of five Fe-bearing minerals in St. Christensen: ferroan dolomite, siderite, pyrite, illite, and chlorite. Figure 10F shows that for the majority of measurements, Fe had a weak, positive relationship with Si. Fe associated with Si is interpreted to represent the presence of clays, such as illite and chlorite. However, the highest Fe measurements corresponded with high Mg and had no relationship with Si. These high Fe-Mg intervals are interpreted to represent ferroan dolomite and siderite formed during secondary dolomitization in the A-1C. Although pyrite was recognized in the core descriptions and identified with XRD, it likely represents only a small portion of

the total Fe variation, as evidence by lack of Fe in high S intervals (Figure 10B). For the most part, increases in Fe appear to accompany increases in Si, Al, and K, evidence that Fe represents variation of the clay fraction of primary clastic deposition in the A-1C. However, high Fe concentrations, which deviate from Si, Al, and K occur in Dreves and David. This is interpreted to reflect precipitation of ferroan dolomite and siderite, or authigenic precipitation of pyrite.

High Sr intervals are interpreted to reflect the presence of celestine formed through post-depositional replacement of anhydrite as well as Sr associated with limestones. Evidence for this includes celestine identified with XRD, the positive correlation between Sr and S displayed in Figure 10C, and corresponding high Sr and S zones in Bruske, St. Christensen, Schultz, and Mutton. However, the lack of spatial correlation of high Sr zones between Dreves, KH 1054, and David suggests that celestine was not deposited concurrently with primary gypsum. Figure 10C shows high Sr related to high Ca, evidence Sr is also associated with calcite in limestones. Additionally, St. Christensen, Schultz, and Mutton display high Sr and low S in limestone intervals, however these intervals cannot be correlated between wells.

The high Zn interval observed in St. Christensen is interpreted to have formed from secondary deposition associated with hydrothermal fluids. No Zn-bearing minerals were identified with XRD, however the high Zn interval in St. Christensen marks the base of the dolomite in this well and Figure 10G indicates a relationship between high Zn and Mg. Additionally, St. Christensen contains abundant “saddle” dolomite and fractured lithofacies consistent with hydrothermal alteration. The relationship between dolomite and Zn along with the lack of spatial correlativity are evidence that Zn trends

formed from secondary depositional processes such as localized alteration from hydrothermal fluids.

No temporal variation is observed in Co, Ti, Ni, Cu, Mo, and Mn in the wells analyzed in this study and therefore are likely in abundances within the standard error limits of the Tracer IV-SD ED-XRF. Additionally, XRD, elemental and TOC cross-plots (Figures 10 and 12) indicate redox sensitive elements have no clear relationship with TOC or the major elements measured in this study.

The association of Si, Al, K, and S with clastic and evaporite minerals, respectively, along with wide-spread correlation of their chemofacies is compelling evidence that fluctuations in these elements reflect changes in the controls on primary deposition. How clastic sediments are transported into a carbonate and evaporite dominated basin is poorly understood. However, lithofacies, mineralogy, and elemental relationships provide some context for clastic deposition in the A-1C. The fine-grained texture and low abundance (< 5 wt%) of the clastic sediments in the A-1C suggests transport over considerable distance. Furthermore, an overall decrease in the quantity of clastic sediments moving from the basin margin to basin center, indicates higher abundance of clastic sediments more proximal to the paleo-shoreline. Schultz and Mutton are an exception to this rule, however, as they contain the highest amount of clastic material and are interpreted as more distal than David (Rine et al. 2017). Additionally, elements representative of siliciclastic minerals (Si, Al, and K) in the A-1C have no relationship with Ti, which is typically associated with ultrastable minerals from continental igneous and metamorphic rocks (Craigie 2018 and the references therein). This is interpreted to mean that clastic material in the A-1C was not derived from a

nearby continental source and was heavily reworked prior to deposition. The likely source of clastic sediments transported over long distances to the Michigan Basin was from highlands to the southeast, created by the Taconic orogeny at the end of the Ordovician period (Rodgers 1971). Figure 20 displays the location of the Michigan Basin in relation to the Taconic highlands during the middle Silurian. High abundances of clastic minerals in Schultz and Mutton can be explained by a southeast to northwest paleo-wind direction, similar to trade winds observed in modern equatorial latitudes. However, high abundances of clastic minerals in Dreves cannot be explained by transport exclusively from eolian processes, thus there was likely terrigenous clastic input from north of the Michigan Basin (Figure 20). These characteristics indicate that the clastic material in the A-1C was likely transported to the basin by a mixture of both fluvial and eolian processes.

Another factor that can influence the temporal variation of clastic sediments in the A-1C is by carbonate dilution. As carbonate sedimentation increases, the percentage of clastic material in the bulk rock volume decreases. Craigie (2018) cited a negative correlation between Ca and Zr as evidence for this process. Figure 10D shows a similar relationship with increasing Si accompanying decreasing Ca and Mg. This is interpreted as evidence that carbonate sedimentation diluted the clastic material in the A-1C.

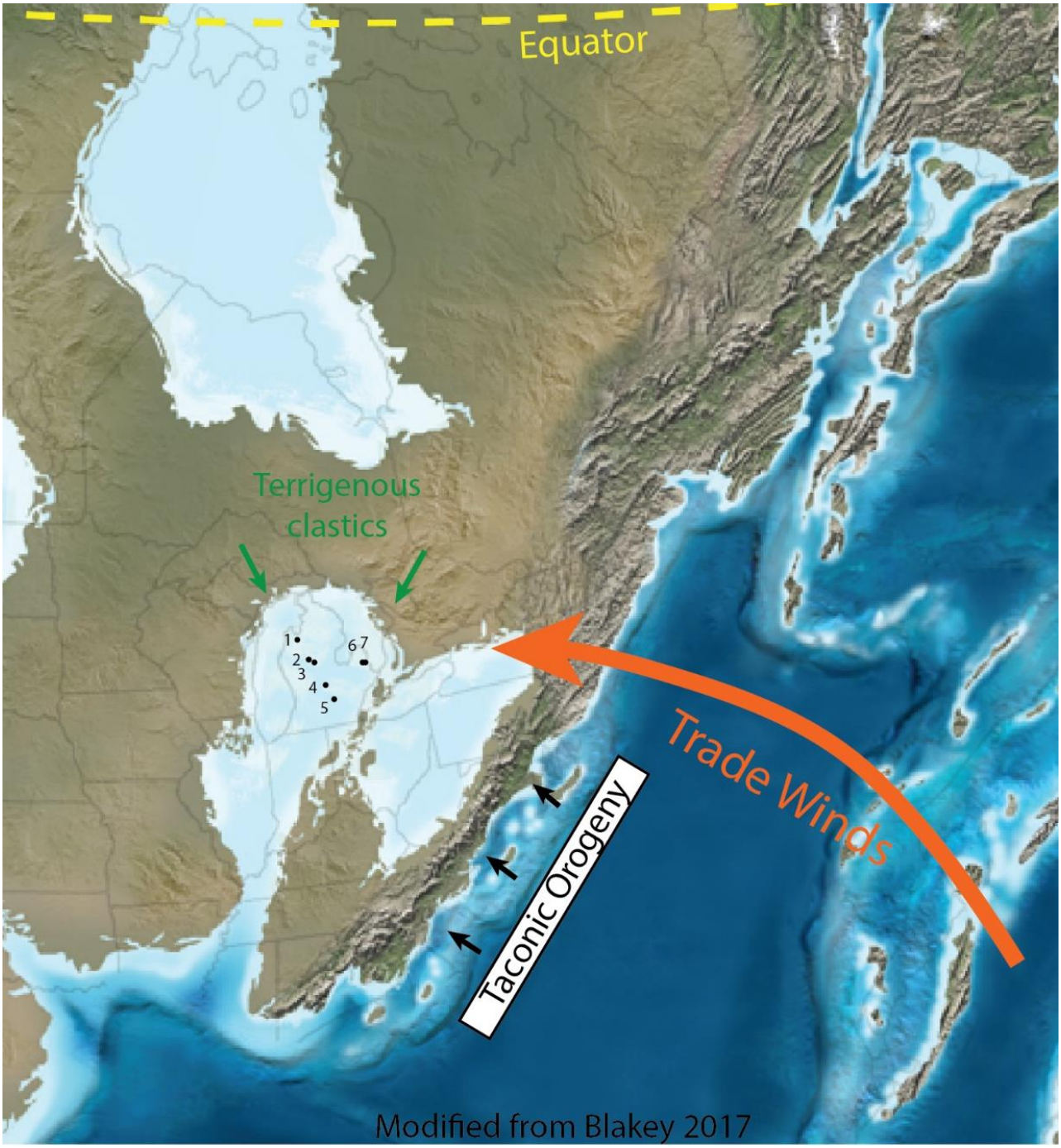

Figure 20: Paleogeographic map of North American during the middle Silurian period with the locations of key wells from this study (modified from Blakey 2017). During this time the Taconic highlands were located to the southeast of the Michigan Basin, and prevailing wind patterns were likely from southeast to the northwest.

Primary gypsum deposition in the A-1C indicates marine-derived fluids that were supersaturated with respect to gypsum. Chemical precipitation of gypsum from sea water is caused by the concentration of sulfate ions through high net evaporation and restriction (Schmalz 1969, Warren 2016). These two conditions are ultimately controlled by climate, basin geomorphology, and a supply of sea water (Schmalz 1969). The anhydritic interval that bifurcates the A-1C was first described at the basin-margin by Gill (1973) as the "Rabbit Ears Anhydrite" (REA). It was later recognized in one basin-center well by Rine et al. (2017) and interpreted as a widespread, time-correlative gypsum precipitation event. Core description and elemental data presented in this study support Rine et al. (2017) observations that the REA represents widespread gypsum precipitation during A-1C deposition. The REA recognized in these previous studies is observed as the regionally correlative, *Type I* S zones *B* and *C* in key wells (Figure 18 and 19), which we will further refer to as the lower and upper REA. Consistent with Rine et al. (2017), the REA is interpreted here to have been deposited when falling sea-level isolated the basin and arid conditions caused widespread gypsum precipitation. The *Type II* S zones identified in key wells (Figure 18 and 19) are likely indicative of the same chemical conditions for gypsum precipitation as the REA. However, they are likely to have occurred on a smaller spatial and temporal scale. These localized conditions likely occurred during brief periods of low sea-level.

Sequence Stratigraphic Model for A-1C Elemental Signatures

Given the conditions needed for gypsum precipitation, the stratigraphic relationship between gypsum and clastic sediments indicates how these two sedimentological systems fluctuate respond in tandem to changing sea-level. The

intervals with high amounts of gypsum and clastic sediments, observed at the top, middle, and bottom of the A-1C, reflect higher abundance of clastic and evaporite sediments corresponding with lower abundance of carbonate sediments during periods of low relative sea-level. Furthermore, intervals with less abundant clastic sediments coincide with low abundances of gypsum, suggesting a decrease in clastic and evaporite sedimentation and an increase in carbonate sedimentation during periods of high sea-level. Figure 21 illustrates a conceptual sequence stratigraphic model showing the relationship between carbonate, evaporite, and clastic sedimentation derived from the observed stratigraphic relationship between Si, Al, K, and S in the A-1C.

During sea level lowstands, the basin likely became periodically isolated from the open ocean as sea-level dropped below the carbonate bank, and high evaporation rates caused the precipitation of gypsum throughout the basin. The maximum regressive surface during lowstand is marked by the deposition of the lower and upper REA. Saline brines coupled with periodic exposure of the carbonate bank and reef tops would have decreased carbonate production by exposure of the benthic carbonate factory, thus reducing the carbonate dilution of clastic sediments. Additionally, as base level dropped, the shoreline would have moved down slope, bringing with it increased deposition of clastic sediments into the basin center. Decreased dilution of the clastics fraction from carbonate sedimentation paired with a distal shift in the paleo-shoreline would have increased in the abundance of clastic minerals in the basin center. Evidence for this increase in clastic and evaporite sediments is the occurrence of high Si, Al, K, and S.

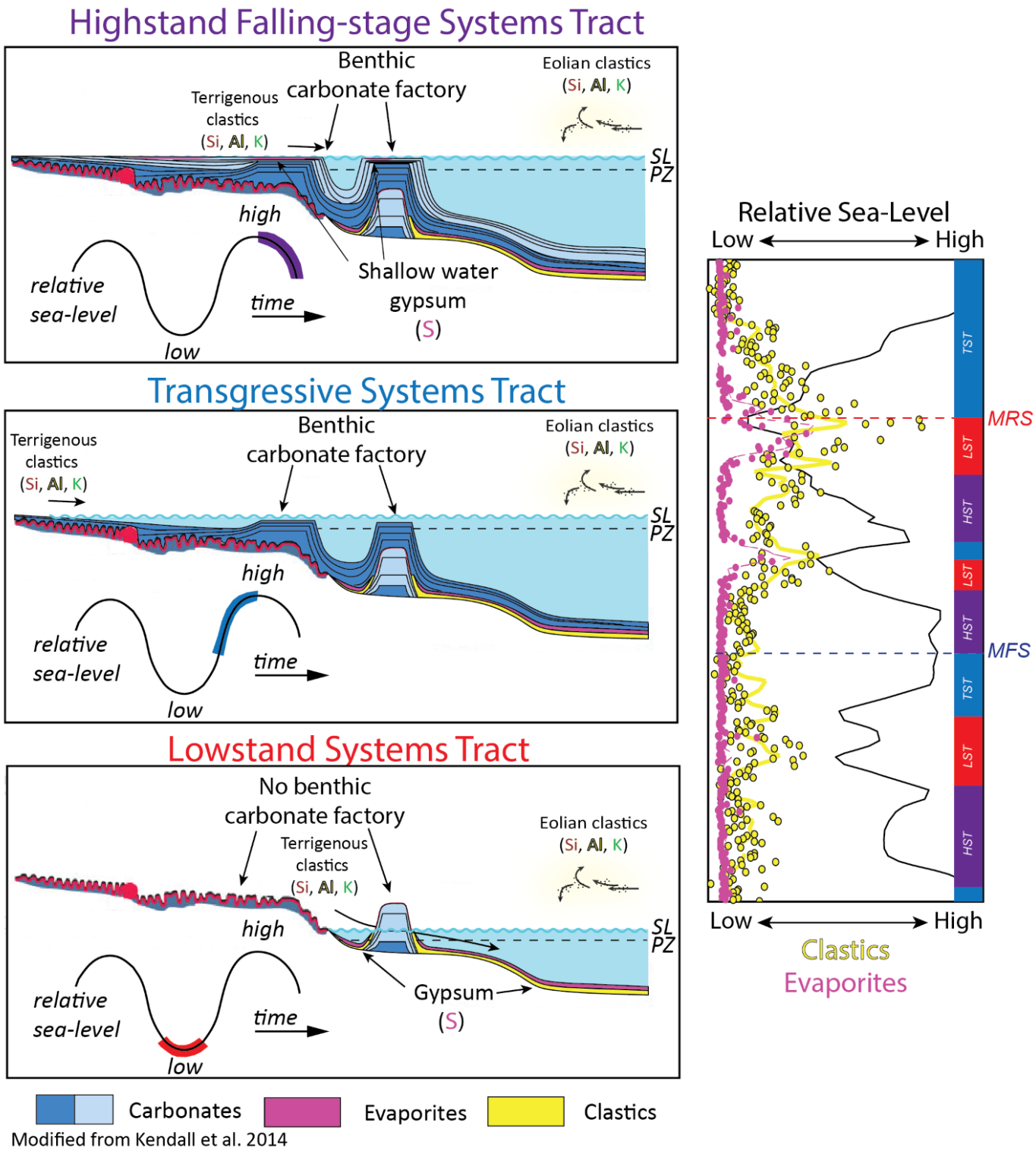

Figure 21: Conceptual model showing the relationship between carbonate, evaporite, and clastic deposition and relative sea-level changes based on the relationship between Si, Al, K, and S observed in the A-1C. Left displays the relative sea-level (SL), photic zone (PZ), and other characteristics of deposition during sea-level lowstand (LST), transgressive(TST), and highstand-falling stand systems tracts (HST). To the right is a generalized curve displaying the abundances of clastics and evaporites in relation to system tracts and the maximum flooding and regressive surfaces (MFS, MRS).

As sea-level transgressed, the basin would have likely reconnected with the open ocean and sea water returned to more normal marine conditions. These conditions would have reestablished the benthic carbonate factory, increasing the carbonate production thus diluting the minor clastic sedimentation during this time. Evidence for increased proximal carbonate sedimentation is found in the thicker (25 – 40 feet) sections in the lower and upper A-1C. Additionally, thicker lower A-1C in Dreves compared to David also supports interpretations of Rine et al. (2017), that the northern slope of the basin was subsiding faster than the southern slope during the transgression in the lower A-1C. Additionally, flooding would have pushed the shoreline more proximal, decreasing the amount of clastic sediments that reached the basin center. Evidence for decreased clastic sedimentation is the occurrence of low Si, Al, and K.

After sea level reached a maximum, benthic carbonate production would have likely been high due to stable, normal marine conditions. Sea-level stabilization along with increased carbonate sedimentation likely began to expend the available accommodation space on the carbonate bank, thus decreasing the dilution effect from carbonate sedimentation and moved locus of clastic input basinward. Evidence for this is the occurrence of gradually increasing upward abundances of Si, Al, and K. This would have allowed for brief periods of restricted conditions where decreased sea water supply to the basin concentrated saline brines in shallow, restricted water, and caused the localized precipitation of gypsum, observed as *Type II* S zones.

This conceptual model explaining the relationship between sea-level and elemental signatures was used to correlate transgressive-regressive cycles (T-R cycles) across the basin. Figure 22 shows the correlation of interpreted relative sea-level from

clastics and evaporites between key wells. Five complete low-order frequency T-R cycles can be correlated between Dreves, Bruske, KH 1054, St. Christensen, and David. Only 3 of these T-R cycles can be correlated to Schultz and Mutton, due to missing core at the top and base of the A-1C in these wells. Twelve complete high-order frequency T-R cycles were correlated between Bruske, KH 1054, St. Christensen, and David. In Dreves, the bottom T-R cycle is absent and only 11 of the 12 high-order T-R cycles were identified. Similar to the low-order T-R cycle correlation, only 6 high-order T-R cycles were identified in Schultz, and 4 high-order T-R cycles in Mutton.

In general, the stratigraphic relationship between clastic and evaporite minerals is consistent across the basin. There is, however, a slight vertical offset between the upper and lower REA with the two maxima for clastic minerals that occur in high-order cycles 8 and 10 (SAK8 and SAK10) in the middle of the A-1C (Figure 22). The offset between clastic and evaporite maxima increases from the northern to the southern slope, with the upper and lower REA occurring below the SAK-cycle maximum. Dreves displays 1-3 feet of offset and Schultz and Mutton display 5-7 feet of vertical offset between maxima. The upper and lower REA occur in a broader high in clastic minerals, however it remains uncertain what causes the offset in maxima between the evaporite and clastics. One possibility is that the stratigraphic position of these two lithologies was influenced by the deposition of carbonate matrix and local variation in carbonate sedimentation likely influenced their observed relative position. Additionally, the high-resolution ED-XRF sampling used in this study likely recorded subtle stratigraphic relationships that have been overlooked in previous chemostratigraphic studies and more research on this topic is needed.

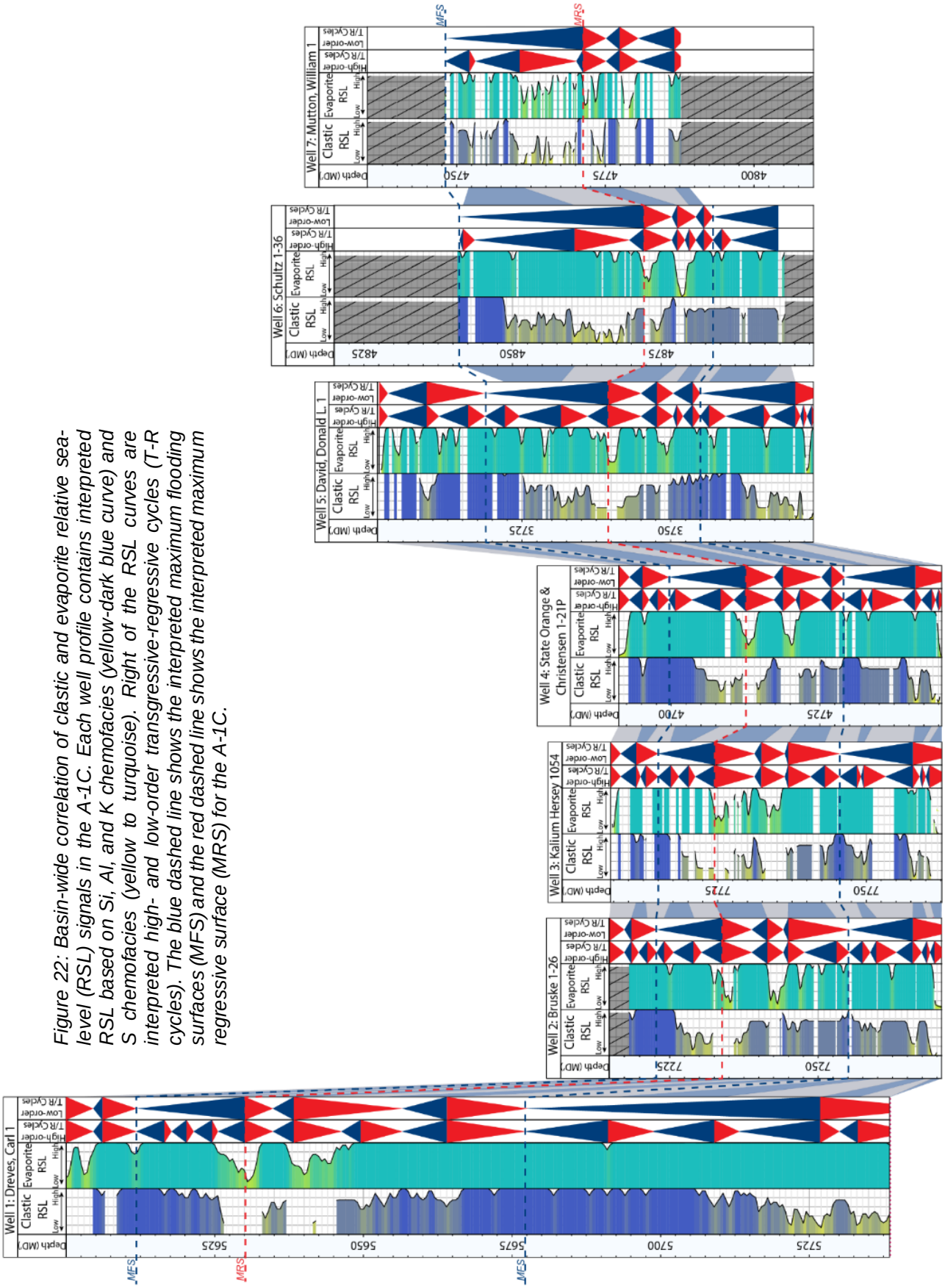

Figure 22: Basin-wide correlation of clastic and evaporite relative sea-level (RSL) signals in the A-1C. Each well profile contains interpreted RSL based on Si, Al, and K chemofacies (yellow-dark blue curve) and S chemofacies (yellow to turquoise). Right of the RSL curves are interpreted high- and low-order transgressive-regressive cycles (T-R cycles). The blue dashed line shows the interpreted maximum flooding surfaces (MFS) and the red dashed line shows the interpreted maximum regressive surface (MRS) for the A-1C.

Trace Elements and Redox Conditions

The lack of an observed relationship between redox sensitive elements Zn, V, Ni, Mo, Mn, Cu, and Co with TOC in the A-1C has several possible explanations. Low concentrations of these elements in both modern and ancient sedimentary basins are interpreted to represent oxic conditions (Algeo & Lyons 2006, Algeo & Rowe 2012). Applying this model to carbonate depositional systems suggests that low abundances of redox sensitive elements in the A-1C is an indication that conditions were relatively oxic and stabile during A-1C deposition. Oxic conditions during the A-1C would contradict a model of deep-water pelagic sedimentation of the REA (Rine et al. 2017), which requires anoxic bottom conditions from density stratification of the water column to preserve deep-water gypsum sediments. Oxic conditions during evaporite deposition is typically interpreted as an indication of relatively shallow water depths (cm to meters), where wind and waves oxygenate the shallow water column and prevent density stratification (Schmalz 1969). If the lack of a relationship between these trace elements and TOC in the A-1C is consistent with other chemostratigraphic studies, then this would indicate relatively shallow water (<20 meters) during A-1C deposition, which is at odds with Rine et al. (2017) interpretations.

An alternative explanation for the low abundance of redox sensitive elements in the A-1C is a limited supply of these elements from sea water due to restricted conditions. Tribovillard et al. (2006) proposes that the primary source of these trace elements is sea water, and Algeo and Lyons (2006) found that anoxia, caused by water-mass restriction in modern semi-restricted basins, concentrates these trace elements in sediments through sulfide precipitation. However, if the degree of basin-restriction

during A-1C deposition was far greater than modern semi-restricted basin, then it is possible that trace elements from the open ocean was never replenished in the Michigan Basin following the deposition of the A-1 Evaporite. This implies that conditions during A-1C deposition may have been anoxic, but the low abundances of trace elements in basin sea water prevented a record of the event in the sediments.

The third explanation for the low abundances of redox sensitive elements in the A-1C is the due to thermal alteration of the organic carbon in the A-1C. Wagenvelt (2015) used geodynamic modeling to quantify the thermal maturation of the Michigan Basin, and found that the A-1C had undergone moderate to high thermal maturation, converting the majority of the organic matter to oil and gas. Due to a higher degree of thermal maturity, it is likely that the TOC values measured with RockEval in this study contain less organic carbon then when first deposited during the A-1C. Therefore, the relationship between trace elements and TOC was significantly altered in the A-1C.

Correlations in Elemental Chemostratigraphy

While the spatial correlations proposed in this study are consistent with available elemental data, an unambiguous chronostratigraphic correlation cannot be accomplished without additional temporal constraint. Correlation of “like” elemental signatures does not necessarily mean these signatures are time correlative. For example, Figure 23 presents two alternative models for the correlation of Si and S between Dreves, Bruske, and KH 1054. Model 1 mirrors the correlations proposed in Figures 18, 19, and 22, where the upper and lower A-1C and REA are observed throughout the basin center. Model 2 proposes that none of the Si and S cycles in Dreves correlate to Bruske and KH 1054, and that the A-1C is divided into the lower A-

1C, REA, middle A-1C, and upper A-1C. While Model 1 has the fewest assumptions, without age constraints both models are plausible, and this scenario highlights the importance of using chronostratigraphy to guide chemostratigraphic correlations.

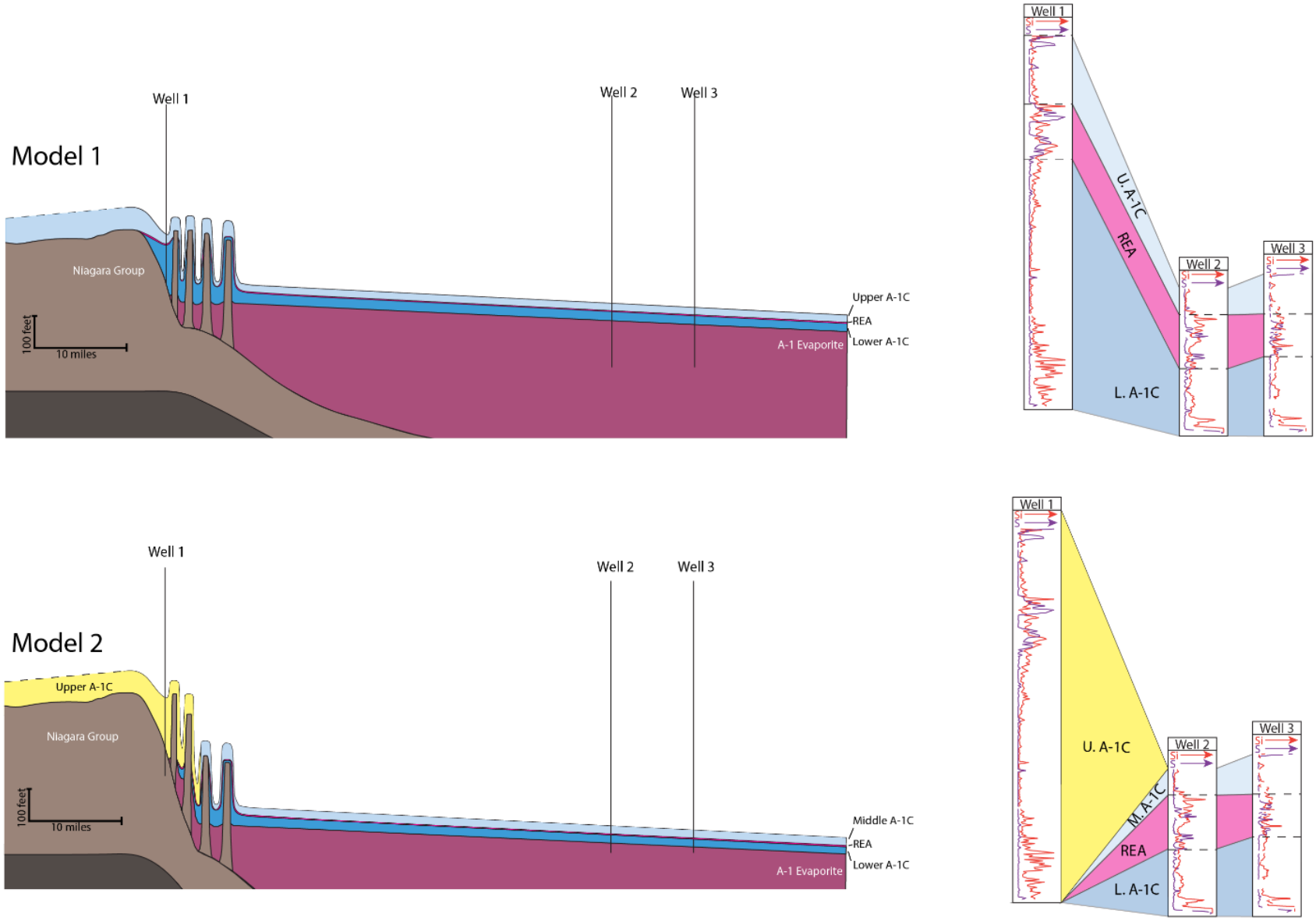

Figure 23: Alternative elemental correlation models for Dreves, Bruske, and KH 1054. Model 1 correlates the upper A-1C, REA, and lower A-1C between these wells while Model 2 divides the A-1C into 4 units, the lower A-1C, REA, middle A-1C, and upper A-1C, with the upper A-1C only occurring in Dreves. These two scenarios highlight the importance of chronostratigraphic data to resolve elemental correlations

CONCLUSIONS

This study represents the first basin-wide chemostratigraphic study of fine-grained carbonate rocks utilizing ED-XRF. With over 9,000 individual geochemical measurements, this dataset is unparalleled in scope and resolution. The data presented permit several important inferences to be made.

(i) Handheld ED-XRF is a quick and inexpensive way to measure the unobservable geochemical variability in homogenous, carbonate mudstones. This efficient technology permits a substantially larger elemental data set than achieved in previous elemental chemostratigraphic studies.

(ii) The signatures of some elements recorded with ED-XRF (e.g. Si, Al, K, and S) in the A-1C are consistent and correlative across the Michigan Basin. This observation suggests that elemental signatures represent significant depositional events and that distal A-1C sediment deposition was subjected to the same controls and conditions.

(iii) The integration of ED-XRF elemental data and XRD mineralogical data is essential to constrain potential geological interpretations. The multiple element-mineral associations observed in the A-1C highlight the importance of identifying element-mineral relationships when making geological interpretations. Examination of element-mineral associations allows for more robust interpretations of changes in the mineral assemblages and recognition of primary detrital minerals from those of a diagenetic origin. The ability to discern between elemental signatures that reflect primary deposition and

diagenetic alterations permits robust stratigraphic correlations, and more meaningful interpretations about sea-level change, sea water chemistry, and sedimentation rates.

(iv) Variations of the visually unobservable, non-carbonate fraction of sediments in this carbonate system was the key to discerning basin-wide sequence stratigraphic and paleogeographic relationships. Major element signatures of Si, Al, K, and S indicate variations in primary deposition of clastic and evaporite sediments in the carbonate-dominated A-1C. The spatial correlativity and the stratigraphic covariance between these elements indicates that intervals with higher abundances of clastic and evaporite minerals represent sedimentation during low relative sea-level. In contrast, intervals with low abundances of Si, Al, K, and S reflect low levels of clastic and evaporite sedimentation during relatively high sea-level. From this relationship, 14 high-order and 6 low-order transgressive-regressive cycles were identified and correlated throughout the Michigan Basin. Interestingly, small (> 2 m) vertical offsets are observed between the maximum regressive surface interpreted from Si, Al, K and S, which suggests that the evaporite and siliciclastic depositional systems are responding to different sedimentological controls at the basin scale. These vertical offsets further exemplify the need for more high-resolution data sets to fully understand the relationship between controls on elemental signatures.

(v) The data presented show that regardless of the high-resolution elemental data set near continuous ED-XRF measurements provide, chronostratigraphic

constraint is still essential. Despite the utility of elemental signatures to inform high-resolution stratigraphic correlations in fine-grained sedimentary carbonates, the precise timing of elemental chemostratigraphic units cannot be resolved without chronostratigraphic data.

REFERENCES

Abdi, H. and Williams, L. J., 2010, Principal component analysis: Wiley Interdisciplinary Reviews: Computational Statistics, Edition 2.4, p. 433-459

Algeo, T. J., Lyons, T. W., 2006. Mo-total organic carbon covariation in modern anoxic marine environments: Implications for analysis of paleoredox and paleohydrographic conditions: Paleoceanography, v. 21, p. 1-23.

Algeo, T. J. and Rowe, H., 2012. Paleoceanographic applications of trace-metal concentration data. Chemical Geology, v. 324, p. 6-18.

Banner, J., 1995, Application of trace element and isotope geochemistry of strontium to studies of carbonate diagenesis. Sedimentology, v.42, p. 805-824.

Bhatia, M., and Cook, K., 1986, Trace element characteristics of graywackes and tectonic setting discrimination of sedimentary basins. Contributions to Mineralogy and Petrology, v.92, p. 181-193

Blakey, R. C., 2017, North American paleogeographic maps: Web https://deeptimemaps.com.

Budros, R., 1974. The stratigraphy and petrogenesis of the Ruff Formation, Salina Group in southeast Michigan: Unpublished M.Sc. thesis, University of Michigan, Ann Arbor, Michigan. p. 1-178

Budros, R. and Briggs, L.I., 1977. Depositional environments of the Ruff Formation (Upper Silurian) in south-eastern Michigan, in: Fischer, J.H. (ed.), Reefs and Evaporites--Concepts and Depositional Models, AAPG Studies in Geology No.5, p. 53-71.

Caplan, M. L. and Bustin, R. M., 1998. Palaeoceanographic controls on geochemical characteristics of organic-rich Exshaw mudrocks: role of enhanced primary production. Organic Geochemistry, 30(2-3), p. 161-188.

Catacosinos, P., Daniels, P., and Harrison, W., 1991, Structure, stratigraphy, and petroleum geology of the Michigan Basin; interior cratonic basins. AAPG Memoir, v.51, p. 561-601.

Coimbra, R., Immenhauser, A., Oloriz, F., Rodriguez-Galiano, V., Chica-Olmo, M., 2015, New insights into geochemical behavior in ancient marine carbonates (Upper Jurassic Ammonitico Rosso): Novel proxies for interpreting sea-level dynamics and palaeoceanography: Sedimentology, v. 62, p. 266-302

Craigie, N. 2015. Application of chemostratigraphy in Cretaceous sediments encountered in the North Central Rub' al-Khali Basin, Saudi Arabia: Journal of African Earth Sciences, v. 104, p. 27-42

Craigie, N., 2018. Principles of elemental chemostratigraphy: A practical users guide. Springer International Publishing, 1st Edition, p. 1-196

Dahl, T.W., Ruhl, M., Hammarlund, E.U., Canfield, D.E., Rosing, M.T. and Bjerrum, C.J., 2013. Tracing euxinia by molybdenum concentrations in sediments using handheld X-ray fluorescence spectroscopy (HHXRF). Chemical Geology, 360, p. 241-251.

Demaison, G. J., and Moore, G. T., 1980, Anoxic environments and oil source bed genesis: AAPG Bulletin 64, p. 1179-1209.

Garber, R., Levy, Y., and Friedman, G., 1987, The sedimentology of the Dead Sea: Carbonates and Evaporites, v. 2, p. 43-57.

Gardner, W. and Bray, E., 1985, Oils and source rocks of Niagaran reefs (Silurian) in the Michigan basin, *in* J.C. Palacas, ed., Petroleum geochemistry and source rock potential of carbonate rocks: AAPG Studies in Geology, v. 18, p. 33-44.

Gill, D., 1973, Stratigraphy, facies, evolution and diagenesis of productive Niagaran Guelph reefs and Cayugan sabkha deposits, the Bell River Mills gas field, Michigan

Basin Unpublished Ph.D. dissertation, University of Michigan, Ann Arbor, Michigan. p. 1-243

Guthrie, J. M., and Ferguson, J. R., 2012, Overview of x-ray fluorescence. Website: http://archaeometry.missouri.edu/xrf_overview.html, University of Missouri Research Reactor.

Hildred, G. V., Ratcliffe, K. T., Wright, A. M., Zaitlin, B. A., Wary, D. S., 2010. Chemostratigraphic applications of low-accommodation fluvial incised-valley settings; an example from the Lower Mannville Formation of Alberta, Canada: Journal of Sedimentary Research, v. 80, p. 1032-1045.

Ibrahim, M. A. A., Sarg, J. F., Hurley, N., Cantrell, D. L., Humphrey, J. D., 2016. Depositional environments and sequence stratigraphy of carbonate mudrocks using conventional geologic observations, multiscale electrofacies visualization, and geochemical analysis: The case of the Tuwaiq Formations in a basinal setting, Saudi Arabia: AAPG Bulletin, v. 101, no. 5, p. 683-714

Jenkins, Ron, 1992. X-ray fluorescence analysis *in* Cahn, R. W., Haasen, P., Kramer, E. J., Materials science and technology: Wiley and Sons, Inc. 1st Edition. p. 620-660.

Kendall, C. G., Moore, P., Viiparelli, E., De Keyser, T. L., Alsharhan, A., Kloot, C. 2014. Analysis of sequence stratigraphic models for the Jurassic Cretaceous sedimentary fill

of the intrashelf basins of the eastern margin of the Arabian Plate: AAPG ACE, Houston, TX

Mesolella, K., Robinson, J., McCormick, L., and Ormiston, A., 1974, Cyclic deposition of Silurian carbonates and evaporites in the Michigan Basin: AAPG Bulletin v.58, no.1, p. 34-62.

Obermajer, M., Fowler, M., Snowdon, L., and Macqueen, R., 2000, Compositional variability of crude oils and source kerogen in the Silurian carbonate-evaporite sequences of the eastern Michigan Basin, Ontario, Canada: Bulletin of Canadian Petroleum Geology v.48, no.4, p. 307-333.

Pearce, T., and Jarvis, I., 1992. Applications of geochemical data to modelling sediment dispersal patterns in distal turbidites: Late Quaternary of the Madeira abyssal plain: Journal of Sedimentary Petrology, v.

Pearce, T., Besly, B., Wray, D., and Wright, D., 1999, Chemostratigraphy: a method to improve interwell correlation in barren sequences – a case study using onshore Duckmantian/Stephanian sequences (West Midlands, UK). Sedimentary Geology, v.124, p. 197-220.

Pearce, T. J., Wray, D., Ratcliffe, K. T., Wright, D. K., Moscariello, A., 2005. Chemostratigraphy of the Upper Carboniferous Schooner Formation, southern North

Sea: Carboniferous Hydrocarbon Geology: The Southern North Sea and Surrounding Onshore Areas, v. 7, p. 147-163

Quye-Sawyer, J., Vandeginste, V. and Johnston, K.J., 2015. Application of handheld energy-dispersive X-ray fluorescence spectrometry to carbonate studies: opportunities and challenges. Journal of Analytical Atomic Spectrometry, 30(7), p. 1490-1499.

Ratcliffe, K. T., Morton, A. C., Ritcey, D. H., Evenchick, C. A., 2006, Whole-rock geochemistry and heavy mineral analysis as petroleum exploration tools in the Bowser and Sustut basins, British Columbia, Canada: Bulletin of Canadian Petroleum Geology, v. 55, no. 4, p. 320-336

Ratcliffe, K. T., Wright, A. M., Montgomery, P., Palfrey, A., Vonk, A., Vermeulen, J., Barrett, M., 2010. Application of chemostratigraphy to the Mungaroo Formation, The Gordon Field, offshore northwest Australia: APPEA Journal 50, p. 371-388.

Ratcliffe, K. T., Wilson, A., Payenberg, T., Rittersbacher, A., Hildred, G. V., Flint, S. S., 2015. Ground truthing chemostratigraphic correlations in fluvial systems: American Association of Petroleum Geologists Bulletin, v. 99, p. 155-180

Ratcliffe, K. T., Playton, T. E., Montgomery, P., Wray, D., Caulfield-Kerney, S., Tohver, E., Hocking, R. M., Haines, P. W., Kirschvink, J., Yan, M., 2017. Using elemental chemostratigraphy on mid-late Frasnian platform-top successions from the Lennard

Shelf outcrops, Canning Basin, Western Australia: SEPM Special Publication No. 107, p 319-331.

Rine, M., Garrett, J., Kaczmarek, S., 2017, A new sequence stratigraphic model for the Silurian A-1 Carbonate (Ruff Formation) of the Michigan Basin *in* Grammer, G. M., Harrison, W. B., Barnes, D. A., Paleozoic stratigraphy and resources of the Michigan Basin: GSA Special papers, v. 531

Rodgers, J. R., 1971. The Taconic Orogeny: GSA Bulletin, v. 82(5), p. 1141-1178

Rousseeuw, P. J., 1987, Silhouettes: a graphical aid to the interpretation and validation of cluster analysis: Journal of Computational and Applied Mathematics, v. 20, p. 53-65

Rowe, H. S., Ruppel, S., Rimmer, S. and Loucks, R., 2009. Core-based chemostratigraphy of the Barnett Shale, Permian Basin, Texas: Gulf Coast Association of Geological Societies Transactions, v. 59, p. 675-686.

Rowe, H., Hughes, N., and Robinson, K., 2012, The quantification and application of handheld energy-dispersive X-ray fluorescence (ED-XRF) in mudrock chemostratigraphy and geochemistry: Chemical Geology, v. 324-325, p. 122-131

Rowe, H., Loucks, R., Kerans, C., 2015, Core chemostratigraphy and elemental geochemistry along a dip-section, Pearsall Formation, Lower Cretaceous, Central to

South TX: Unconventional Resources Technology Conference Paper. http://archives.datapages.com/data/urtec/2015/2154897.htm

Sageman, B., and Lyons, T., 2004, Geochemistry of fine-grained sediments and sedimentary rocks, in Mackenzie, F. (ed.) Sediments, Diagenesis, and Sedimentary Rock. Treatise on Geochemistry, v.7. Elsevier, Amsterdam, p. 115-158.

Schmalz, R. F., 1969, Deep-water evaporite deposition: A genetic model: AAPG Bulletin v. 53, p. 798-823

Tribovillard, N., Algeo, T. J., Lyons, T., Riboulleau, A., 2006, Trace metals as paleoredox and paleoproductivity proxies: An update: Chemical Geology v. 232, p. 12-32

Turner, B. W., Treanton, J. A., Slatt, R. M., 2016, The use of chemostratigraphy to refine ambiguous sequence stratigraphic correlations in marine mudrocks. An example from the Woodford Shale, Oklahoma, USA: Journal of the Geological Society, London, 173. 854-868.

Van Grieken, R. E., Markowicz, A. A., 2001, Handbook of x-ray spectrometry: Marcel Dekker, Inc. 2nd Edition. p. 151-179, 181-291

Wagenvelt, K. A., 2015, Thermal history of the Michigan Basin: Results from thermal maturation data and geodynamic modelling: Unpublished M.S. Thesis, Western Michigan University, Kalamazoo, Michigan. p. 1-154

Warren, J., 2016, Evaporites: A Geological Compendium. Springer International Publishing, 2nd edition, 1813 pp.

Wright, A. 2009, ED-XRF spectroscopy user guide: User Manual, Bruker Elemental. Kennewick, Washington

APPENDIX 1

Salina A-1 Carbonate Background

The Michigan Basin is an intracratonic basin located in middle North America that covers all of Michigan and parts of Wisconsin, Illinois, Indiana, Ohio, and Canada (122,000 mi^2) (Catacosinos et al. 1991). The extent of the basin is defined by the Wisconsin Arch to the west, the Kankakee Arch to the southwest, the Findlay Arch to the southeast, the Algonquin Arch to the east, and the Canadian Shield to the north-northeast, with the deepest part of the basin located in the lower peninsula, west of the Saginaw Bay (Catacosinos et al. 1991). In the Wenlock and Ludlow epochs of the Silurian period, the Michigan Basin was a semi-restricted depression located in tropical to sub-tropical latitudes (20-25°S) that promoted the cyclic deposition of carbonate and evaporate sequences (Budros & Briggs 1977). Based on the current understanding of middle to late Silurian stratigraphic relationships in the Michigan Basin, evaporite and carbonate deposition occurred contemporaneously, with periods of high relative sea-level favoring carbonate deposition (Niagaran, A-0 Carbonate (Cain Formation), A-1 Carbonate (Ruff Formation), and A-2 Carbonate; Mesolella et al. 1974). Conversely, periods of relative sea-level low, when the basin was restricted, favored deposition of evaporites (A-1 Evaporite, A-2 Evaporite, and B Evaporite) (Figure 1, Mesolella et al. 1974). Deposited in the middle Silurian, the Guelph Dolomite is composed of barrier reef carbonates that rimmed the northern and southern margins of the basin and transition distally to large pinnacle reefs on the shelf slope (Figure 1, Budros and Briggs 1974). During this time, the basin was less restricted to the open ocean allowing the sustained growth of the carbonate factory at pinnacle and barrier reef complexes. Starting in the

late Silurian, a relative sea-level drop resulted in the deposition of the regressive A-0 Carbonate, which transitioned to anhydrite and salt of the A-1 Evaporite (Mesolella et al. 1974). Following evaporite deposition, a rise in sea-level reestablished the carbonate factory at the barrier and pinnacle reef complexes, depositing the A-1 Carbonate. However, during this time the Michigan Basin was likely semi-restricted, evidence for which is the dominance of algal buildups and lack of open-marine organisms common during Niagaran deposition (Mesolella et al. 1974). Termination of A-1 Carbonate deposition is marked by a thick package of anhydrite, and halite associated with the A-2 Evaporite, which was likely due to another sea-level drop and restriction of the basin (Mesolella et al. 1974). Following drawdown during A-2 Evaporite deposition, the basin experienced a sea-level rise and resumption of carbonate deposition with the A-2 Carbonate (Figure 24). However, during this time the basin lacked the biota of Niagara and A-1 Carbonate and contains no apparent reef build-ups (Mesolella et al. 1974).

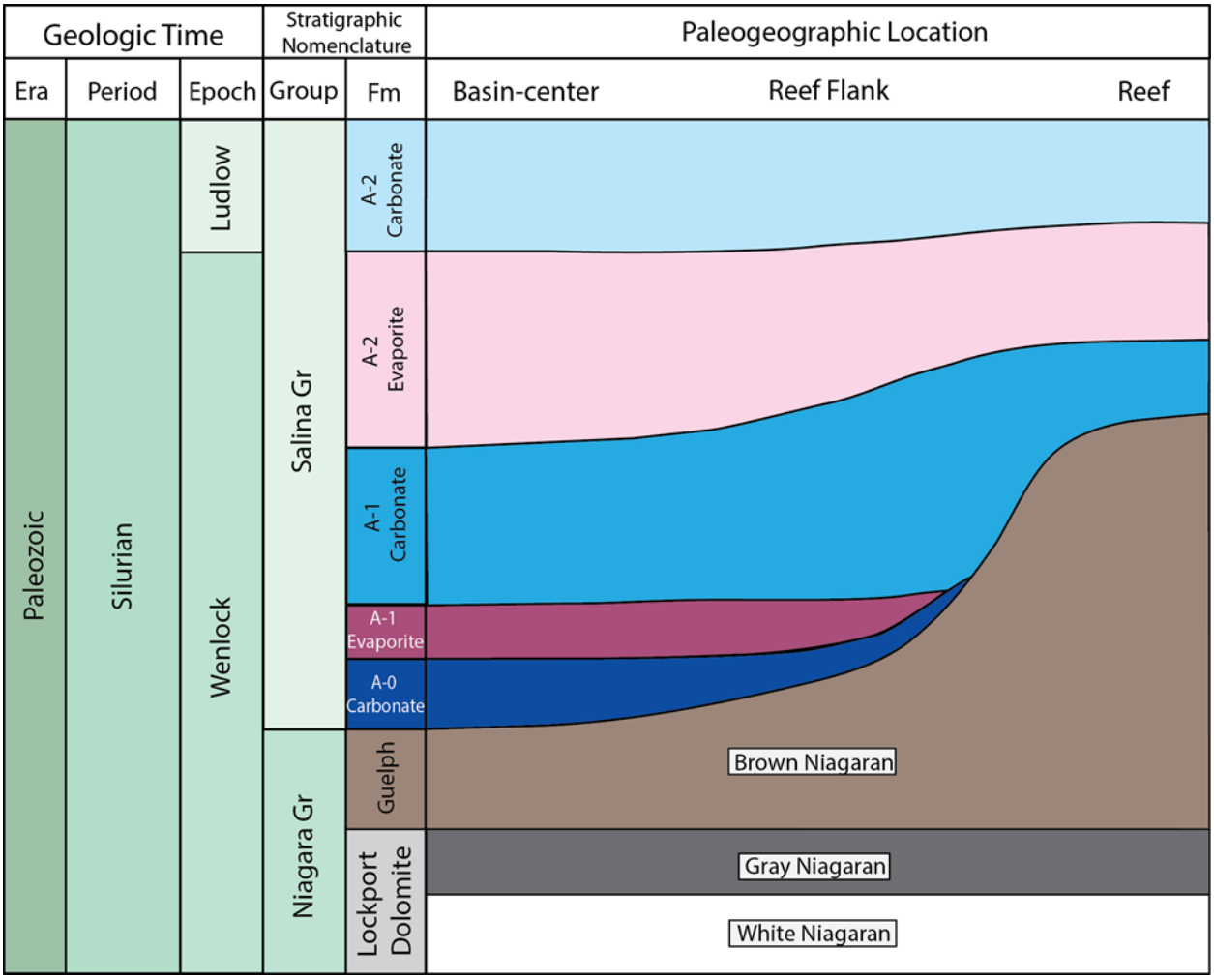

Figure 24: Stratigraphic nomenclature of the Wenlock to Ludlow Epochs of the Silurian in the Michigan Basin. (Modified from Gill, 1973 and Budros & Briggs 1974).

Rine et al. (2017) subdivides the A-1C into three different units: 1) Lower A-1 Carbonate, 2) the “Rabbit Ears Anhydrite” and 3) Upper A-1 Carbonate. Based on their proposed sequence stratigraphic model, the Lower A-1 Carbonate was mostly deposited in a transgressive systems tract (TST) marked by basin-center laminite accumulation followed by deposition in a highstand systems tract (HST) marked by increased carbonate production from the A1 carbonate factory (Rine et al. 2017). This HST was followed by a regressive phase of deposition, falling stage systems tract (LST), during which the basin

became restricted enough to deposit a basin-wide gypsum layer, known as the “Rabbit Ears Anhydrite” (REA) (Rine et al. 2017). The Upper A-1 Carbonate marks another TST and the return of the carbonate factory along the basin margin. This transgression was likely the closest the basin was to the normal marine conditions before a subsequent HST and transition to the A-2 Evaporite (Rine et al. 2017).

Rine et al. (2017) observed predominately observed pelagic carbonate mudstones which they called “poker chip” laminites in Bruske, the one basin-center well they examined. Along with “poker-chip” lithofacies, they identified and correlated the REA from the basin center to the reef flanks (Rine et al. 2017). Rine et al. 2017 interpreted the correlation of the REA from the reef flanks to the basin center as evidence that the A-1C deposited in over 100 m of water depth.

APPENDIX 2

Energy Dispersive X-Ray Fluorescence Spectroscopy Theory

Handheld Energy Dispersive X-Ray Fluorescence (ED-XRF) is an analytic technique that rapidly quantifies a suite of elements based on their fluorescence under radiation. ED-XRF emits an X-ray beam that collides with an electron of an element in the sample material, leaving a vacancy in the atom's inner electron shell. The device then measures the wavelength of the photons emitted when an outer shell electron fills this vacancy. Since all elements have a unique electron structure, the difference in binding energies between shells and the resulting release of energy in the form of a photon is specific to that element. ED-XRF emits radiation at a sample to eject electrons from the atoms of the sample's elements and measures the energy and amount of returning radiation to determine the concentration of those elements. While the theory of ED-XRF is, for the most part, consistent between instruments, the ED-XRF system outlined below refers to the Bruker Tracer IV-SD, ED- XRF (Wright 2009).

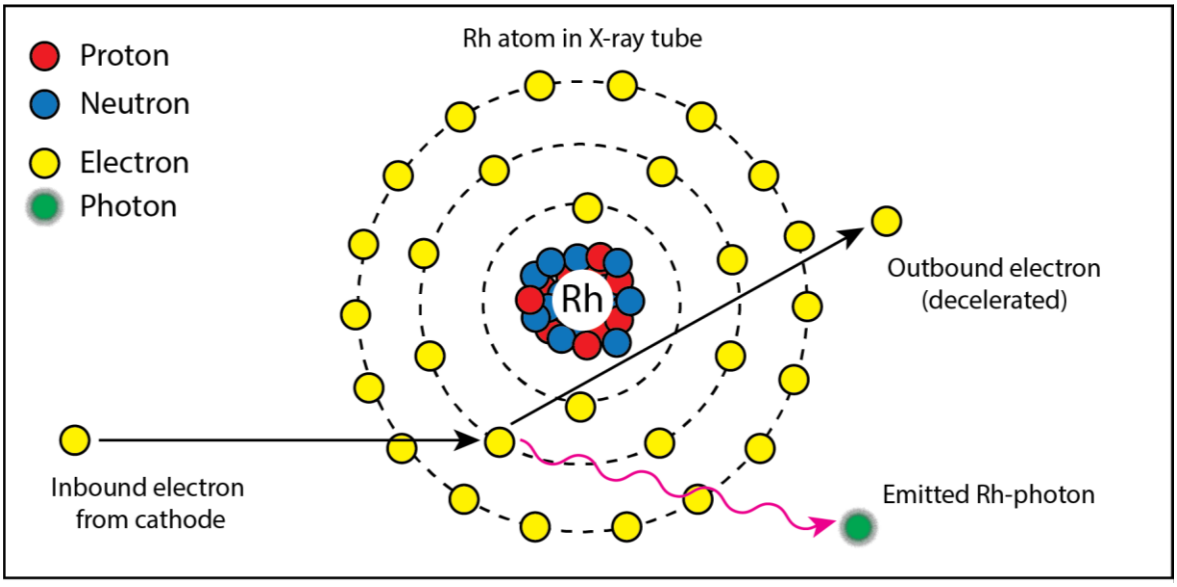

Figure 25: Diagram displaying the interactions that occur within the instrument X-ray tube to produce a spectrum of photons known as a Bremsstrahlung continuum (Modified from Wright 2009)

The ED-XRF system has three major components: 1) the X-ray tube, 2) sample, and 3) the silicon detector. The X-ray tube produces an X-ray beam by bombarding a rhodium (Rh) target with electrons generated at a cathode, composed of tungsten wire (Guthrie & Ferguson 2012). The beam is comprised of photons is produced by two unique interactions that take place as electrons hit the Rh target. Incoming electrons either ionize Rh atoms, producing a photon with a wavelength characteristic to the energy needed for an outer shell electron to fill the vacancy left by the ejected electron, (inelastic scattering). Conversely, they are slowed as they move through the atoms nucleus (elastic scattering). These two interactions produce an X-ray beam composed of photons with a broad range of wavelengths known as a Bremsstrahlung continuum (Figure 25) (Van Grieken & Markowicz 2002). Depending on what elements are present in the sample, the range of photon wavelengths in the X-ray beam can be altered by adjusting the voltage and current settings of electrons striking the Rh-tube or with different composition filters.

The next component in the ED-XRF system involves the interaction between the incident photons from the Rh-tube and the atoms of the elements being analyzed in the sample. If the incident photon from the ED-XRF collides with an electron positioned in an inner shell of the atom (K-shell), an electron is ejected (Figure 26). This only happens when the energy of the incident photon is greater than the binding energy of the electron (Van Grieken & Markowicz 2002). The vacancy left in the K-shell leaves the atom unstable and the atom responds in one of two ways. The simplest path to reestablishing stability is by transitioning an electron from one of its higher-energy, outer shells (L, M, or N) down to the inner K-shell. During this process, a photon with a wavelength equal to the energy difference between the two shells is released (Figure 26) (Van Grieken &

Markowicz 2002). An electron can also be ejected from the L or M shells and filled by electrons from higher shells, emitting photons with characteristic wavelengths. These transitions can be written in Siegbahn notation where the first letter, K, L, or M, indicates the shell where an electron was ejected, and the subscript α, β, and γ indicates the probability of the resulting transition from a higher shell, from most to least respectively. Regardless of which transition occurs, the wavelengths of the photons emitted are characteristic to each element, which allows for identification of elements by measuring the returning wavelength (Jenkins 1992)

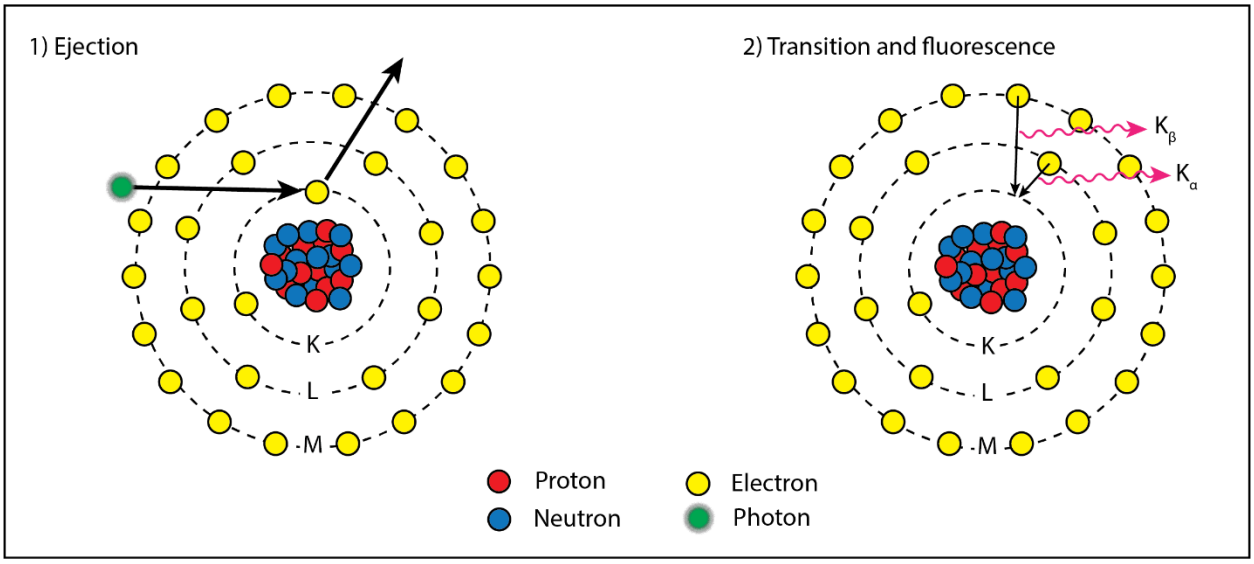

Figure 26: The 2-step process by which atoms in a sample fluoresce under ED-XRF. An incoming photon ejects an electron from the atoms inner shell. This vacancy in filled by an electron from either the L - or M-shell resulting in the release of energy in the form of a photon with a characteristic wavelength to the atom of that element and the shell which the electron came from.

The final component in the ED-XRF system is the detector within the Tracer IV-SD that reads the returning photons from the sample. The detector functions by measuring the number of electrons ejected from the ED-XRF's silicon detector lattice by the returning photons. The number of ejected electrons from the lattice coincides with the energy of the

returning photons, which the detector counts and converts to a digital signal to produce a spectrum of photon counts of different wavelengths. These photon counts can be converted to elemental concentrations, if a calibration file has been created for the sample using another analytical technique.

Rowe et al. 2012 Calibration Curves: Major Elements Setting

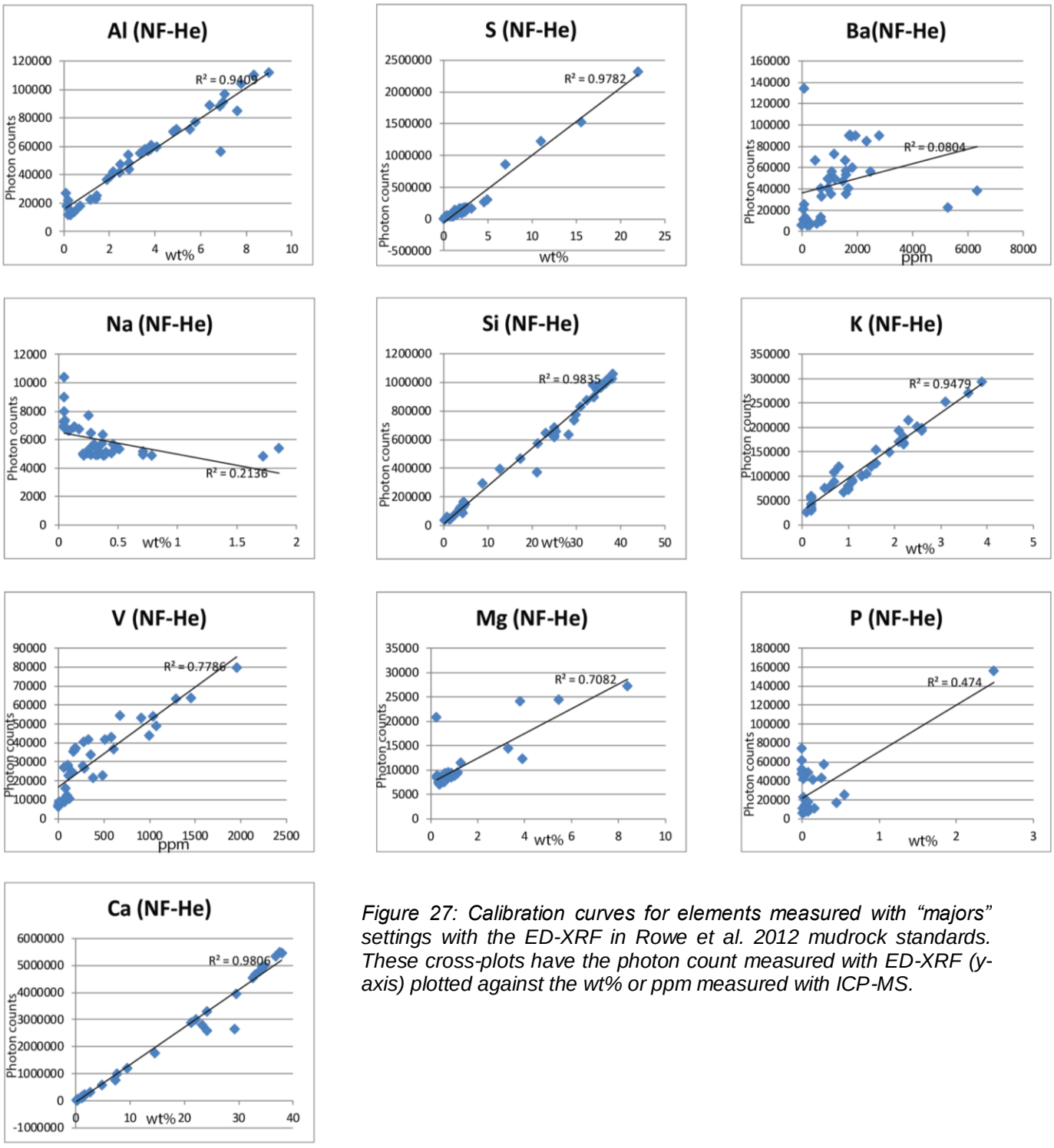

Figure 27: Calibration curves for elements measured with "majors" settings with the ED-XRF in Rowe et al. 2012 mudrock standards. These cross-plots have the photon count measured with ED-XRF (y-axis) plotted against the wt% or ppm measured with ICP-MS.

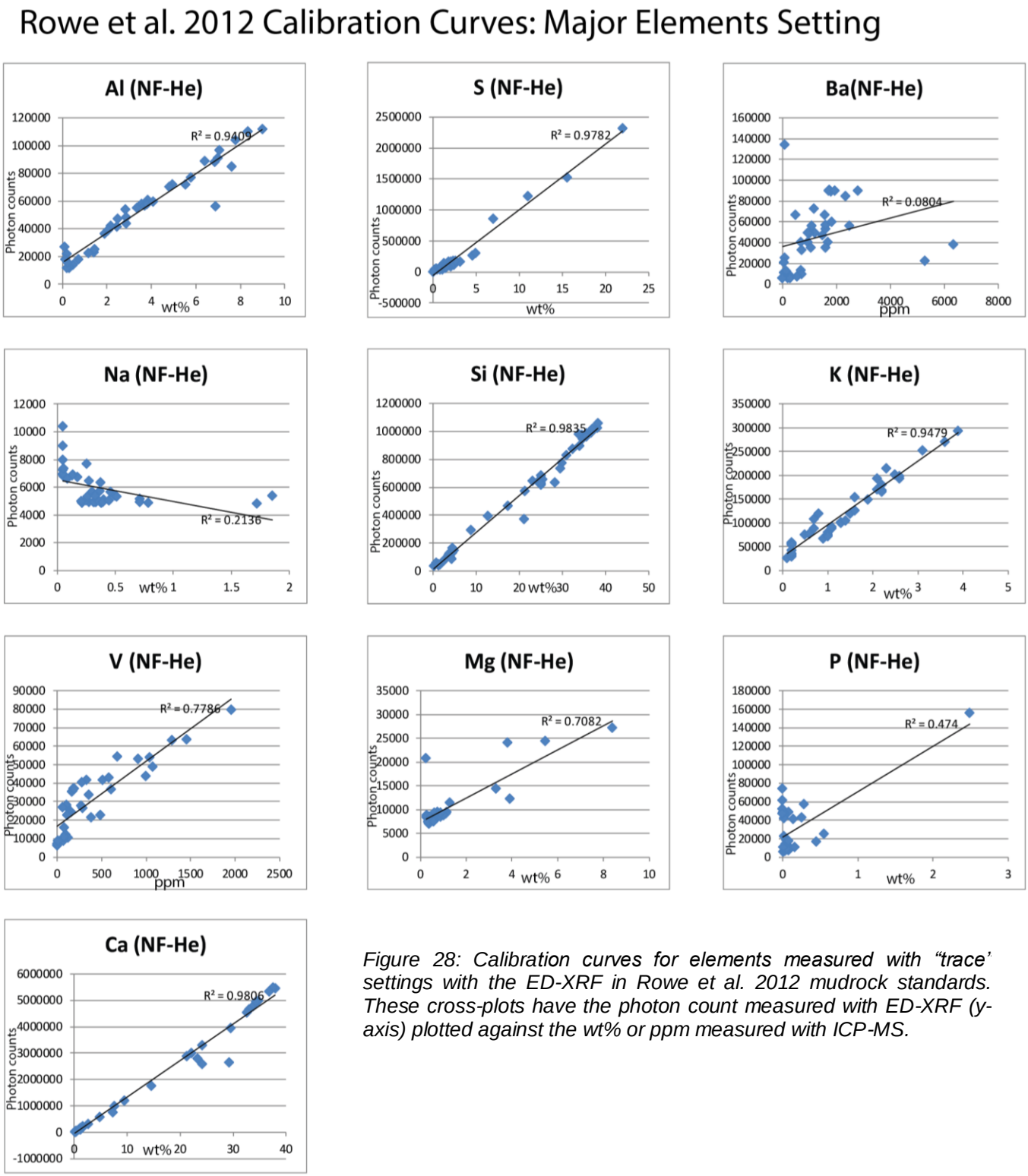

Figure 28: Calibration curves for elements measured with "trace' settings with the ED-XRF in Rowe et al. 2012 mudrock standards. These cross-plots have the photon count measured with ED-XRF (y-axis) plotted against the wt% or ppm measured with ICP-MS.

Figures 27 and 28 display calibration curves from Rowe et al. 2012 mudrock samples used to determine the accuracy of ED-XRF settings for this study.

Figure 29 displays the detectable limits of each element measured in this study. These values come from the Wright 2009 Bruker Tracer IV-SD user manual.

Ne (gas)*	Na	Mg	Al	Si	P	S	Cl
0.5%	0.5%	0.05%	150 ppm	100 ppm	100 ppm	100 ppm	75 ppm
K	**Ca**	**Sc**	**Ti**	**V**	**Cr**	**Mn**	**Co**
75 ppm	75 ppm	75 ppm	60 ppm	30 ppm	15 ppm	15 ppm	8 ppm
Ni	**Cu**	**Zn**	**As**	**Se**	**Sr**	**Mo**	**Rh**
5 ppm	4 ppm	4 ppm	3 ppm	3 ppm	1 ppm	1 ppm	1 ppm
Ag	**Cd**	**Sn**	**Sb**	**Ba**	**Ta**	**W**	**Au**
1 ppm	1 ppm	1 ppm	1 ppm	60 ppm	1 ppm	3 ppm	3 ppm
Hg	**Tl**	**Pb**	**Th**	**U**			
3 ppm	1 ppm	3 ppm	3 ppm	3 ppm			

Detection limits in a pure silicate

Ne (gas)*	Na	Mg	Al	Si	P	S	Cl
0.5%	0.5%	0.05%	150 ppm	100 ppm	100 ppm	100 ppm	75 ppm
K	**Ca**	**Sc**	**Ti**	**V**	**Cr**	**Mn**	**Co**
75 ppm	75 ppm	75 ppm	75 ppm	75 ppm	75 ppm	60 PPM	60 PPM
Ni	**Cu**	**Zn**	**As**	**Se**	**Sr**	**Mo**	**Rh**
60 PPM	60 PPM	3 ppm	3 ppm	3 ppm	1 ppm	1 ppm	1 ppm
Ag	**Cd**	**Sn**	**Sb**	**Ba**	**Ta**	**W**	**Au**
1 ppm	1 ppm	1 ppm	1 ppm	75 ppm	1 ppm	3 ppm	3 ppm
Hg	**Tl**	**Pb**	**Th**	**U**			
3 ppm	1 ppm	3 ppm	3 ppm	3 ppm			

Detection limits in a normal silicate

Figure 29: : Detection limits for elements measured with the Bruker Tracer IV-SD in normal (natural) and pure silicate material (Wright 2009)

APPENDIX 3

EDS Elemental Maps

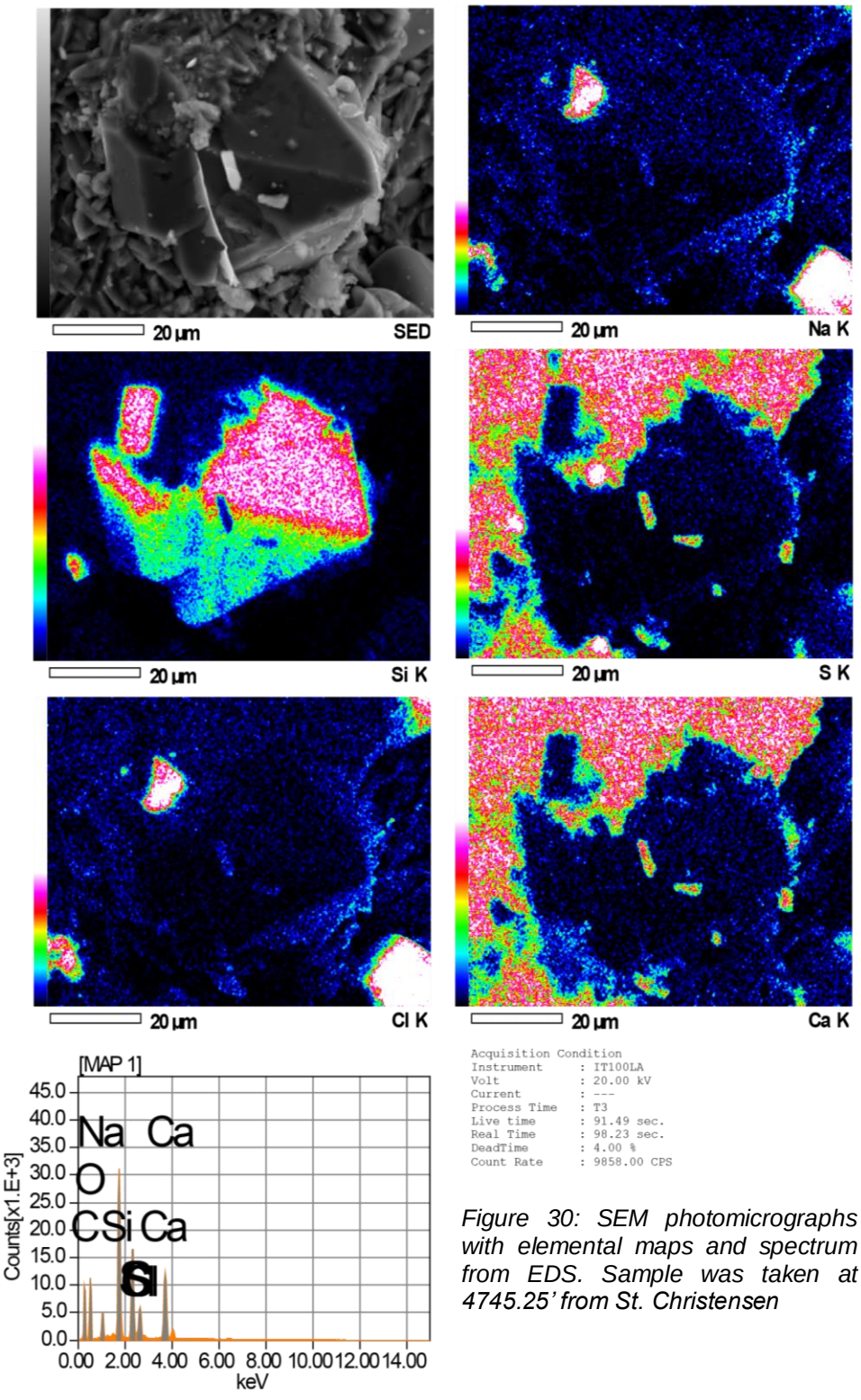

Figure 30: SEM photomicrographs with elemental maps and spectrum from EDS. Sample was taken at 4745.25' from St. Christensen

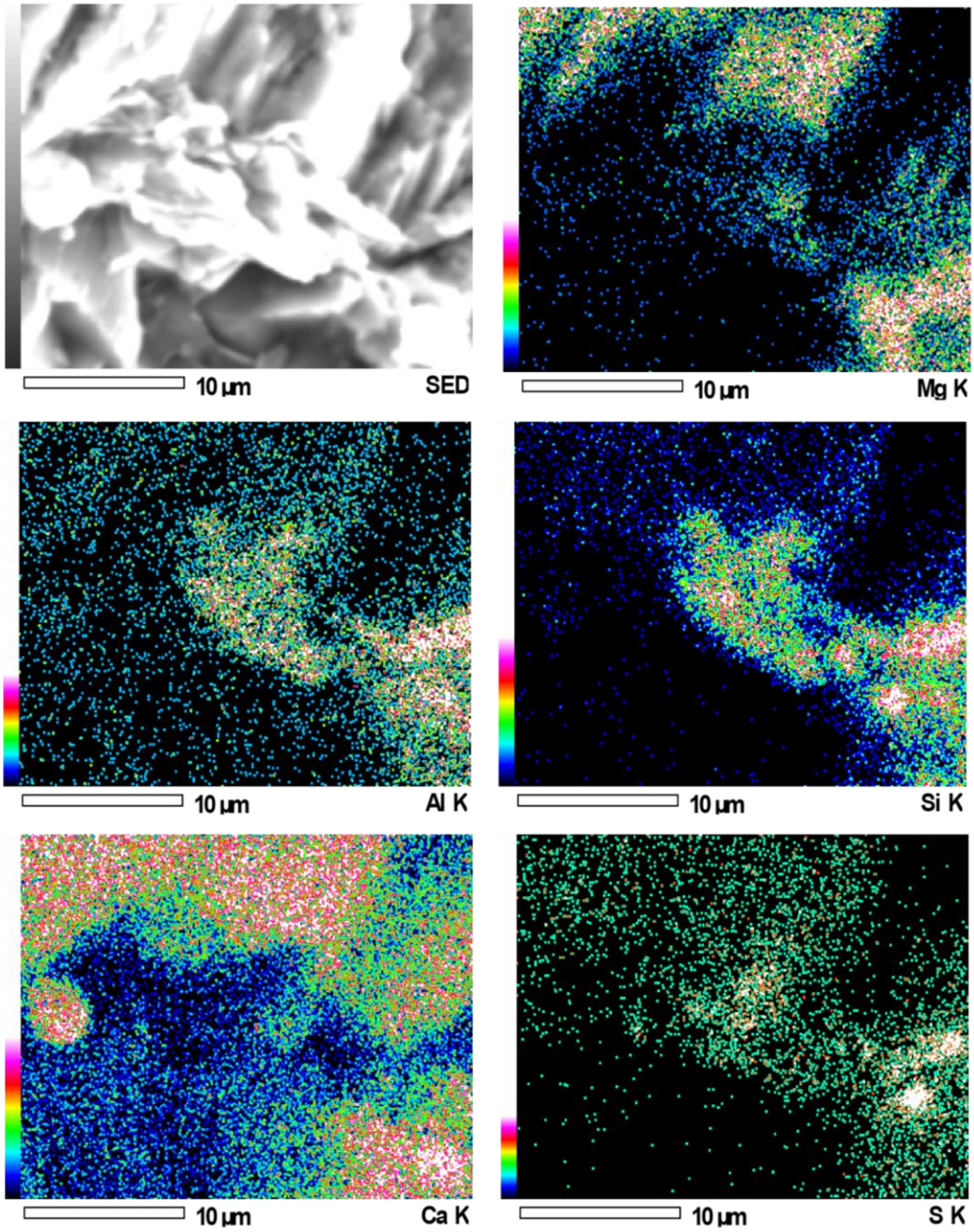

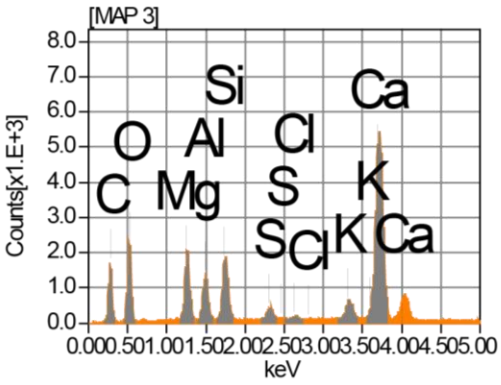

Acquisition Condition
Instrument : IT100LA
Volt : 20.00 kV
Current : ---
Process Time : T3
Live time : 77.15 sec.
Real Time : 78.63 sec.
DeadTime : 2.00 %
Count Rate : 2763.00 CPS

Figure 31: SEM photomicrographs with elemental maps and spectrum from EDS. Sample was taken at 4708.5' from St. Christensen.